The Astrophysical Journal, 954:155 (23pp), 2023 September 10 https://doi.org/10.3847/1538-4357/acdf5e

SN 2018gj: A Short Plateau Type II Supernova with Persistent Blueshifted Ha Emission

Rishabh Singh Teja[1,2], Avinash Singh[3], D. K. Sahu[1], G. C. Anupama[1], Brajesh Kumar[4], Tatsuya Nakaoka[3], Koji S Kawabata[3], Masayuki Yamanaka[5], Ali Takey[6], and Miho Kawabata[7]
[1] Indian Institute of Astrophysics, II Block, Koramangala, Bengaluru-560034, Karnataka, India; rishabh.teja@iiap.res.in, rsteja001@gmail.com
[2] Pondicherry University, R.V. Nagar, Kalapet, Pondicherry-605014, UT of Puducherry, India
[3] Hiroshima Astrophysical Science Center, Hiroshima University, Higashi-Hiroshima, Hiroshima 739-8526, Japan
[4] Aryabhatta Research Institute of Observational Sciences, Manora Peak, Nainital-263001, Uttarakhand, India
[5] Kagoshima University, Amanogawa Galaxy Astronomy Research Center, 1-21-35, Korimoto, Kagoshima 890-0065, Kyushu-Okinawa, Japan
[6] National Research Institute of Astronomy and Geophysics (NRIAG), Helwan 11421, Cairo, Egypt
[7] Department of Astronomy, Kyoto University, Kitashirakawa-Oiwake-cho, Sakyo-ku, Kyoto 606-8502, Japan
Received 2023 March 30; revised 2023 June 15; accepted 2023 June 16; published 2023 September 1

Abstract

We present an extensive, panchromatic photometric (UV, optical, and near-IR) and low-resolution optical spectroscopic coverage of a Type IIP supernova SN 2018gj that occurred on the outskirts of the host galaxy NGC 6217. From the *V*-band light curve, we estimate the plateau length to be $\sim 70 \pm 2$ days, placing it among the very few well-sampled short plateau supernovae (SNe). With *V*-band peak absolute magnitude $M_V \leqslant -17.0 \pm 0.1$ mag, it falls in the middle of the luminosity distribution of the Type II SNe. The color evolution is typical to other Type II SNe except for an early elbow-like feature in the evolution of $V-R$ color owing to its early transition from the plateau to the nebular phase. Using the expanding photospheric method, we present an independent estimate of the distance to SN 2018gj. We report the spectral evolution to be typical of a Type II SNe. However, we see a persistent blueshift in emission lines until the late nebular phase, not ordinarily observed in Type II SNe. The amount of radioactive nickel (^{56}Ni) yield in the explosion was estimated to be $0.026 \pm 0.007\, M_{\odot}$. We infer from semianalytical modeling, nebular spectrum, and 1D hydrodynamical modeling that the probable progenitor was a red supergiant with a zero-age-main-sequence mass $\leqslant 13\, M_{\odot}$. In the simulated hydrodynamical model light curves, reproducing the early optical bolometric light curve required an additional radiation source, which could be the interaction with the proximal circumstellar matter.

Unified Astronomy Thesaurus concepts: Observational astronomy (1145); Type II supernovae (1731); Hydrodynamical simulations (767); Red supergiant stars (1375)

Supporting material: data behind figure, machine-readable tables

1. Introduction

Massive stars ($\geqslant 8\, M_{\odot}$) reach their life-cycle termination in violent explosions termed as core-collapse supernovae (CCSNe). On the basis of their observable properties, viz., spectral lines and light curves, CCSNe are further divided into various subclasses. The absence of hydrogen Balmer lines in the spectrum puts a supernova (SN) into the Type I class, whereas the presence of these features allows it to be classified as a Type II SN. Type I class is further subdivided with the presence or absence of He I λ 5876 (Ib or Ic; Minkowski 1941; Filippenko 1997). Based on their light-curve shape, Type IIs are further classified under Type IIP and IIL subclasses. A plateau-like constant luminosity period of about 100 days in the light-curve evolution means the SN is of the Type IIP (plateau) class. While a "linear" decline from maxima in the light curve denotes the SN to be of Type IIL (linear) class (Barbon et al. 1979). Although there are observed dissimilarities in the light curves of Type IIP and Type IIL classes, it is still unsettled if the two classes are intrinsically different. In many sample studies, it is noticed that the Type II subclasses (IIP and IIL) form a continuous sequence (Anderson et al. 2014a; Sanders et al. 2015; Singh et al. 2018; de Jaeger et al. 2019; Pessi et al. 2019). In contrast, few studies present subtle differences in these subclasses both photometrically and spectroscopically (Arcavi et al. 2012; Faran et al. 2014a, 2014b). Recent studies with larger samples seem to favor the continuous population of these events (Galbany et al. 2016; Rubin et al. 2016; Gutiérrez et al. 2017). Apart from these typical classes, there have been numerous instances where narrow emission spectral features are superimposed over usual broad emission features (Stritzinger et al. 2012; Taddia et al. 2013; Smith et al. 2014; Gangopadhyay et al. 2020; Ransome et al. 2022) in the SN spectra. These events are interacting SNe and known as IIn SNe (Filippenko 1997).

With the advent of various night-sky surveys, viz., Zwicky Transient Facility (Bellm et al. 2019), Asteroid Terrestrial-impact Last Alert System (ATLAS; Tonry et al. 2018), Gaia (Gaia Collaboration et al. 2016), All-Sky Automated Survey for Supernovae (ASAS-SN, Kochanek et al. 2017), etc., we see an enormous number of discoveries and extensive follow-up related to SNe. From the numerous observational (Elmhamdi et al. 2003a; Anderson et al. 2014a) and theoretical modeling studies (Sukhbold et al. 2016; Curtis et al. 2021), it is well established that the average plateau length in type IIP SNe is around 100 days. However, there are cases when the plateau length is found to be longer ($\geqslant$120 days, Sahu et al. 2006; Pastorello et al. 2009; Yang et al. 2021) or shorter ($\leqslant$65 days, Hiramatsu et al. 2021; Teja et al. 2022) than the typical value. SNe with a longer plateau duration are mostly found to be low-

luminosity IIP. A moderate range of progenitor masses (10–15 $M_{\odot}$, Spiro et al. 2014) have been deduced by modeling them, and these masses corroborate with the direct detection of progenitors (Smartt 2009). Nevertheless, Type IIP events with plateau lengths less than 70 days are rare in synthesized models and observations. The occurrence of short plateau events is very small (∼4% of all type IIP SNe) in binary population synthesis and single progenitor models (Eldridge et al. 2018; Hiramatsu et al. 2021). The small number of well-studied short plateau objects is insufficient to constrain these rates quantitatively. Thus, any addition to the sample of short plateau events will further improve our understanding of Type II SNe.

The shorter plateau length in Type IIP SNe is usually explained by considerable stripping of the hydrogen envelope. The stripping of the outer hydrogen layer is possible in all mass ranges of red-supergiants (RSGs) via various mechanisms, viz., wind mass loss, presence of a secondary star, episodic mass losses, etc. Some theoretical works have shown high-mass RSGs as progenitors of short plateau SNe (Dessart et al. 2010; Sukhbold et al. 2016; Hiramatsu et al. 2021) as, with the usual single-star evolutionary scenario with "typical" mass loss, only the more massive stars are able to achieve stronger winds required to strip enough hydrogen to cause a shorter plateau. However, there are reasons to believe otherwise, where it is possible to get a shorter plateau if the multiplicity (Eldridge et al. 2018) or extensive mass loss in lower-mass RSG is considered (Teja et al. 2022). In a study by Sollerman et al. (2021), the progenitor of the short plateau object SN 2020jfo was solely detected in the F814W band of the Hubble Space Telescope (HST), estimating its mass to range from 10 to 15 $M_{\odot}$. The lack of detection of the progenitor in the bluer bands indicated the progenitor as a cool and red star. Further, the observational upper mass for Type IIP progenitors is $\lesssim$19 $M_{\odot}$ (Van Dyk 2017), although the masses of RSGs observed in the Local Group galaxies have been found to range up to 25 $M_{\odot}$ (Smartt et al. 2009; Rodríguez 2022), leading to the missing mass "RSG problem." Massive RSGs as progenitors for the short plateau could address the "RSG problem" (Hiramatsu et al. 2021), although, in general, there is no consensus with regards to the statistical significance of the RSG problem (Eldridge et al. 2013; Davies & Beasor 2020; Kochanek 2020).

With the high cadence of modern sky surveys, quite a few of the short plateau SNe are discovered soon after the explosion. Early detection of these events provides essential information about the late-stage evolution of the progenitor and its immediate surrounding. The "flash ionization" features seen in some of these events are interpreted as the presence of circumstellar material (CSM) in their immediate vicinity (Gal-Yam et al. 2014). The flash ionization feature has been observed in about 18% of the SNe II, at ages < 5 days (Khazov et al. 2016). With the increasing number of SNe observed early enough, the fraction of SNe showing flash ionization features is also increasing (>36%, Bruch et al. 2023), indicating the presence of CSM close to the explosion site is common in Type II SNe (Morozova et al. 2018). Other observational features such as narrow emission lines, high-velocity (HV) absorption features in spectra, and enhanced luminosity in light curves (Bullivant et al. 2018; Singh et al. 2019; Zhang et al. 2022) also reveal the presence of spatially confined CSM, most probably originating from enhanced mass loss from the progenitor shortly prior to the explosion.

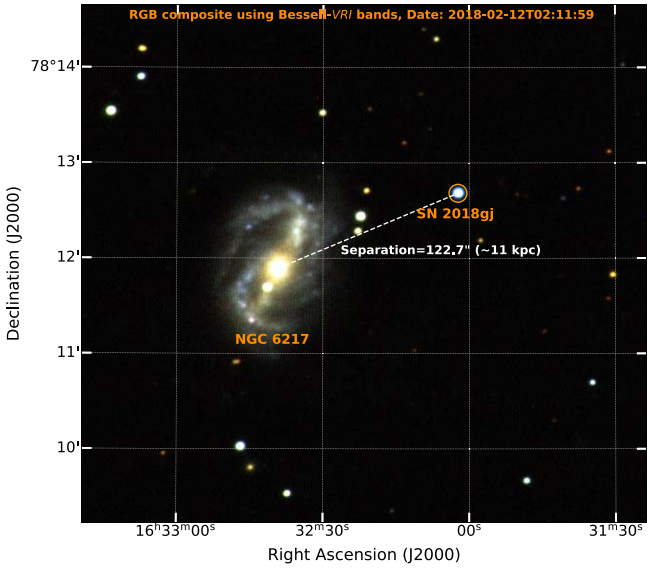

Figure 1. Location of SN 2018gj in the host NGC 6217. The dashed violet line marks the separation between the host center and SN. The image is a red, green, and blue color composite utilizing Bessell's *V*, *R*, and *I* filters.

The evidence of CSM in Type IIP is usually seen early on with ionized lines, narrow emission lines, HV absorption features in spectra, and enhanced luminosity in light curves (Bullivant et al. 2018; Singh et al. 2019; Zhang et al. 2022). Furthermore, it has been established that sometimes only a few of these features are present while others are missing altogether (Andrews et al. 2019; Dong et al. 2021). However, alternate pathways regarding the initial rise times and enhanced luminosity are being studied theoretically. The detailed studies of the hydrogen-rich layer in 3D models (Goldberg et al. 2022) could also reveal the initial behavior of the peak if other shreds of evidence are scarce.

This work presents detailed spectroscopic and photometric observations of SN 2018gj along with the analytical and hydrodynamical modeling to infer properties of probable progenitor. The paper has been divided as follows: Section 2 briefly describes the data acquisition and reduction process. The analysis of the apparent and the bolometric light curve is given in Section 3.2. This section also utilizes semianalytical light-curve modeling for approximate estimates of progenitor properties. The spectral evolution from the photospheric phase to the nebular phase is presented in Section 4. Further, in Section 5, we attempt to estimate the progenitor evolution history, its properties, explosion parameters, etc., using complete 1D hydrodynamical modeling. We briefly discuss the implications of our work and aspects related to consistent blueshifted emission lines in Section 6 and provide a conclusion in the subsequent section.

2. Data Acquisition and Processing

The discovery of SN 2018gj, in the outskirts of the barred spiral galaxy NGC 6217 (about 122″ or ∼11 kpc away from the center of the host galaxy; Figure 1), was reported on 2018 January 14 (2458132.91 JD) at (J2000), R.A., $\alpha = 16^{\circ}32'02\overset{''}{.}40$, and decl., $\delta = +78^{\circ}12'41\overset{''}{.}13$ (Wiggins 2018). Immediately after the discovery, it was classified as a Type IIb SN with the possibility of it being a Type IIP SN (Bertrand

2018). Later on, it was classified as a young Type II SN (Kilpatrick 2018). We started an extensive follow-up campaign in optical–near-IR (NIR) photometry and spectroscopy, which continued for about 300 days after the discovery. An imager cum spectrograph, the Himalaya Faint Object Spectrograph (HFOSC) mounted on the 2 m Himalayan Chandra Telescope (HCT) of the Indian Astronomical Observatory (IAO; Prabhu 2014), Hanle, India, was used for optical photometry and spectroscopy. It is equipped with a liquid nitrogen-cooled 2×4 k pixels SITe CCD chip. With a pixel size of 15 μm, it provides a plate scale of $0\farcs296$ pixel^{-1}. The gain and readout noise of the CCD are 1.22 e^-/ADU and 4.87 e^-, respectively. Near Infrared (NIR) data were acquired with the Hiroshima Optical and Near-InfraRed Camera (HONIR; Akitaya et al. 2014) installed at the 1.5 m Kanata Telescope operated by the Hiroshima Astrophysical Science Center of Hiroshima University. The NIR Arm has a HgCdTe VIRGO-2K array with 2×2 k pixels (pixel size 20 × 20 μm, plate scale of $0\farcs295$ pixel^{-1}) with 11.6 e^-/ADU and 24 e^- gain and readout noise, respectively. In addition to the science frames, we obtained several biases and twilight flat frames.

We pre-processed optical raw data using standard tasks in `IRAF` implemented using a custom pipeline `RedPipe` (Singh 2021) built upon `PyRAF` to correct for bias, flat-field, and cosmic rays. The observed multiple frames were aligned and coadded in respective bands to improve the signal-to-noise ratio. Standard star fields PG 1633 + 009, PG 2213-006, and SA 110 from Landolt (1992) were observed on four nights under photometric conditions to calibrate secondary standards in the SN field. We used DAOPHOT 3 (Stetson 1987) to perform point-spread function (PSF) photometry on the standard fields. The average atmospheric extinction coefficient for the site from Stalin et al. (2008) and the standard stars with a brightness range of $12.02 \leqslant V \leqslant 16.25$ mag and color range of $-0.22 \leqslant B - V \leqslant 2.53$ mag were used for calibration of secondary standards. As the SN was relatively isolated in its host galaxy, the SN magnitude was extracted using PSF photometry. The extracted magnitudes were then calibrated differentially with respect to the secondary standard in the SN field. The SN magnitude in *UBVRI* bands are listed in Appendix A. The NIR data was also reduced using the standard IRAF tasks. The secondary stars for *J*, *H*, and *Ks* bands were calibrated using the magnitudes provided by the Two Micron All Sky Survey catalog (Skrutskie et al. 2006). The SN magnitudes in *JHKs* bands are listed in Appendix A.

Further, we supplemented our photometry data using public archive images from the UltraViolet/Optical Telescope (UVOT; Roming et al. 2005) on board Neil Gehrels Swift Observatory (Gehrels et al. 2004) in the *UVW*2, *UVM*2, *UVW*1, *UVU*, *UVB*, and *UVV* bands. The archival images were reduced using High Energy Astrophysics Software (v6.27) package with the latest calibration database for the *UVOT* instrument, following the methods described in Poole et al. (2008), Brown et al. (2009). The SN magnitude was extracted using `UVOTSOURCE` task with an aperture size of 5″ for the source and a similar aperture size to extract the background counts. The final *UVOT* magnitudes were obtained in the Vega system and are tabulated in Table 4. We also obtained photometry in ATLAS-*o* band (AB-magnitude) from ATLAS forced photometry server (Tonry et al. 2018; Smith et al. 2020).

The low-resolution spectroscopic (∼ 10 Å) data was obtained with HFOSC using a setup consisting of $1\farcs92$ slit with grisms, Gr7 (3800 − 6840 Å) and Gr8 (5800 − 9350 Å) during 2018 January 14 (JD 2458132.5) to 2018 October 31 (JD 2458423.1). The log of spectroscopic observations is given in Table 6 and marked in Figure 2. The spectra of arc lamps and spectrophotometric standards were also obtained for wavelength and flux calibration, respectively. The standard tasks in IRAF were used for spectral data reduction. The observed spectroscopic data were corrected for bias, and the 1D spectra were extracted using the optimal extraction algorithm (Horne 1986). Wavelength calibration was performed using the dispersion solutions obtained utilizing arc lamp spectra. Night-sky emission lines were used to check the accuracy of wavelength calibration, and small shifts were applied wherever necessary. The instrumental response was corrected using the observed spectrophotometric standards. The response curves obtained during nearby nights were used for those nights where standard star observations were unavailable. The flux-calibrated spectrum in both the grisms was combined to obtain a single flux-calibrated spectrum. The spectra were then scaled to the calibrated *UBVRI* magnitudes to bring them to an absolute flux scale.

3. Analysis

3.1. Host Properties

The preferred redshift (z) and distance (D) of NGC 6217 are 0.00454 ± 0.00001 and 19.61 ± 1.37 Mpc, respectively, and are referenced from NASA/IPAC Extragalactic Database (NED).[8] Other distance estimates exist with a great scatter ranging from 15 to 35 Mpc (Bottinelli et al. 1984; Tutui & Sofue 1997). The SN was located in the outskirts of the probable host NGC 6217 ($9'13\farcs8$ W and $47\farcs4$N implying $\sim 2'$ separation from the host's center). To check the veracity of its association with NGC 6217, an independent estimate of the distance to the SN was made using the expanding photosphere method (EPM; Kirshner & Kwan 1974; Schmidt et al. 1992; Hamuy et al. 2001). The detailed methodology and calculations are presented in Appendix B. The dilution factors were adopted from Hamuy et al. (2001), Dessart & Hillier (2005), and Vogl et al. (2019). We found that the distances estimated using constrained explosion epochs and nonconstrained explosion epochs varied as much as by 3 Mpc. The average distances using all three dilution factors are 15.7 ± 1.7 Mpc (nonconstrained explosion epoch) and 17.5 ± 4.1 Mpc (constrained explosion epoch). The errors quoted are due to the scatter in the different measurements for three filter sets and three dilution factors. The distance of the SN estimated using EPM is in agreement with the distances given in NED for NGC 6217 and establishes the association of the SN with NGC 6217.

From IRSA-Galactic Dust Reddening and Extinction map (Schlafly & Finkbeiner 2011), the Galactic line-of-sight reddening toward the SN location is given as $E(B-V) = 0.0375 \pm 0.0002$ mag. Weak Na ID absorption was detected in the spectra at the redshift of the host galaxy with a pseudo-equivalent width (pEW) of 0.36 Å, averaged over the first five spectra. Using Equation (9), Poznanski et al. (2012), we find a host reddening value of $E(B-V) = 0.04 \pm 0.02$ mag. Hence, throughout this work, we adopt a total line-of-sight reddening value $E(B-V) \approx 0.08 \pm 0.02$ mag.

[8] http://ned.ipac.caltech.edu/

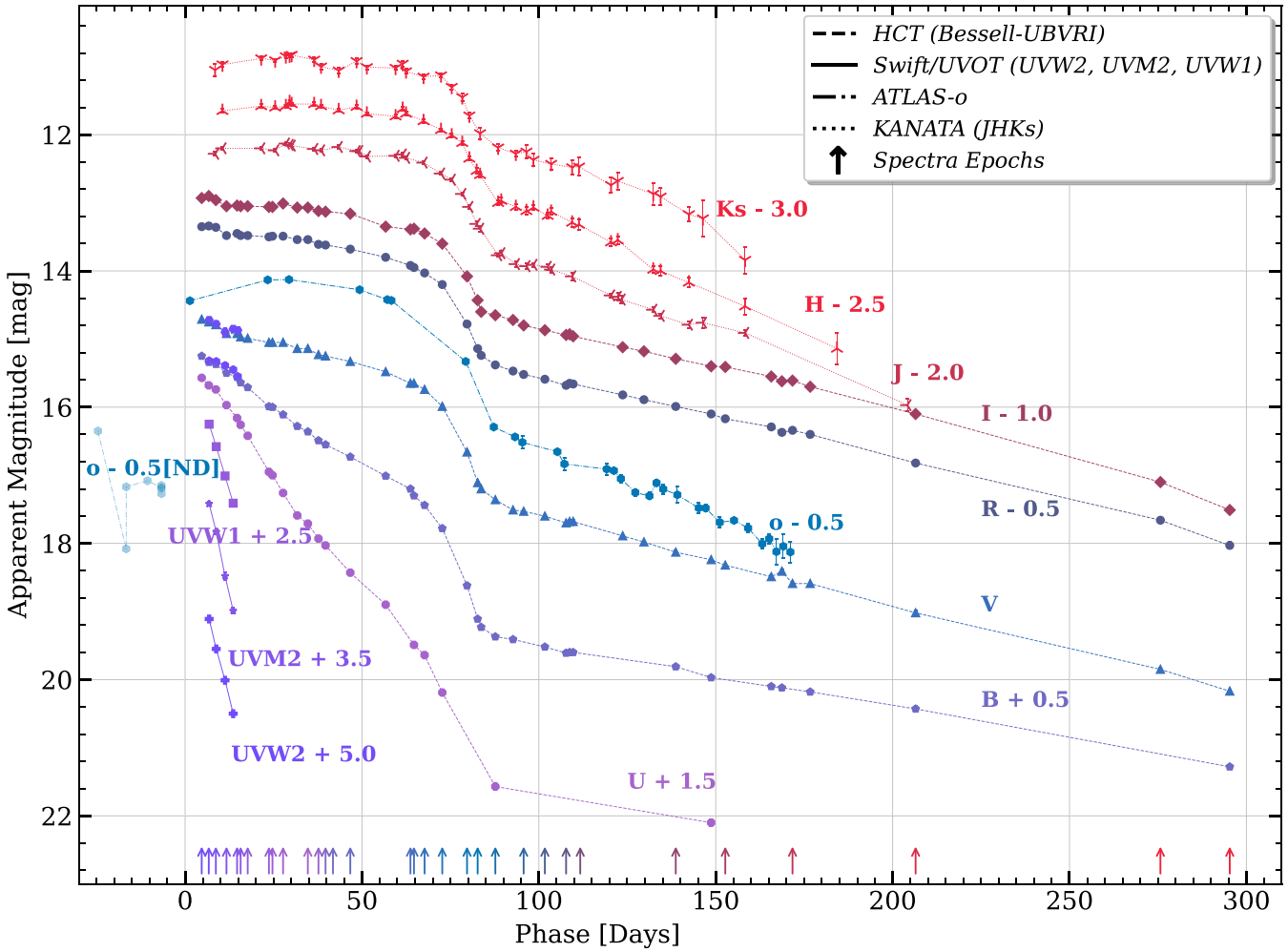

Figure 2. Photometric data for SN 2018gj spanning ∼300 days post-discovery. Corresponding spectral epochs are marked along the abscissa. [Violet pentagon markers overplotted on *V* and *B* bands are from Swift *UVV* and *UVB* bands, respectively.]

3.2. Light-curve Analysis

The last nondetection of SN 2018gj was on 2018 January 7.9 (JD 2458126.4) in the Gaia photometry, up to the limiting magnitude of ∼21.5 in *G-Gaia* filter (AB magnitude system), and was discovered on 2018 January 10.7 (JD 2458129.2). Using this last nondetection and the first detection of SN 2018gj, the explosion epoch is constrained as 2018 January 9.3 (∼JD 2458127.8) ± 1.4 days. This explosion epoch has been used throughout this work, and all the phases are reported with respect to it. The panchromatic light-curve evolutions of SN 2018gj in UV, optical, and NIR bands are presented in Figure 2. UV light curves in *UVW*2, *UVM*2, and *UVW*1 bands span a period of ∼14 days post-explosion; NIR light curves span up to 180 days whereas the optical light curve extends until ∼297 days. In all the light curves, we find a clear transition from the slowly declining (almost constant) light-curve phase to the radioactive nickel-powered phase toward the end. During this transition, in visual bands, we see a drop of ⩾1.5 mag.

During the plateau phase, the light curves decline at different rates in different wave bands. In the *U* filter, we observe the sharpest decline with 6.44 ± 0.03 mag $(100\,\mathrm{d})^{-1}$. As we move toward the redder wavelengths, we find the decline rate slows down to 3.39 ± 0.03 mag $(100\,\mathrm{d})^{-1}$ in *B*, 1.26 ± 0.02 mag $(100\,\mathrm{d})^{-1}$ in *V*, 0.79 ± 0.02 mag $(100\,\mathrm{d})^{-1}$ in *R*, and 0.64 ± 0.02 mag $(100\,\mathrm{d})^{-1}$ in *I*. The decline is even slower in the NIR wavelength regime with 0.37 ± 0.02 mag $(100\,\mathrm{d})^{-1}$ in *J*, but the decline rate increases slightly as we go toward redder bands with 0.42 ± 0.06 mag $(100\,\mathrm{d})^{-1}$ in *H* and ultimately 0.50 ± 0.07 mag $(100\,\mathrm{d})^{-1}$ in *Ks* band. We find the slowest decline to be in the *J* filter. It is also noteworthy that, in the radioactive decay tail phase, the decline rate trend reverses with the slowest decline observed in *B* band 0.90 ± 0.01 mag $(100\,\mathrm{d})^{-1}$, and it is almost the same in *V*, *R*, and *I* bands as 1.33 ± 0.01 mag $(100\,\mathrm{d})^{-1}$, 1.14 ± 0.02 mag $(100\,\mathrm{d})^{-1}$, and 1.26 ± 0.02 mag $(100\,\mathrm{d})^{-1}$ respectively. We find the late-phase light-curve decline rates to be much higher in the NIR bands as 1.86 ± 0.07 mag $(100\,\mathrm{d})^{-1}$ in *J*, 2.58 ± 0.11 mag $(100\,\mathrm{d})^{-1}$ in *H*, and 2.12 ± 0.24 mag $(100\,\mathrm{d})^{-1}$ in *Ks* bands. During the late phase, the light curve in the *H* band declined at the fastest rate.

3.3. V-band Light Curve

After correcting for extinction, the apparent *V*-band magnitudes were transformed to absolute magnitudes using a distance modulus, $\mu = 31.46 \pm 0.15$ mag (using the preferred distance of 19.61 ± 1.37 Mpc as given in NED). Even though the initial rise in the bluer bands is missed, we see the light curve getting brighter during the first two observations in the *I*

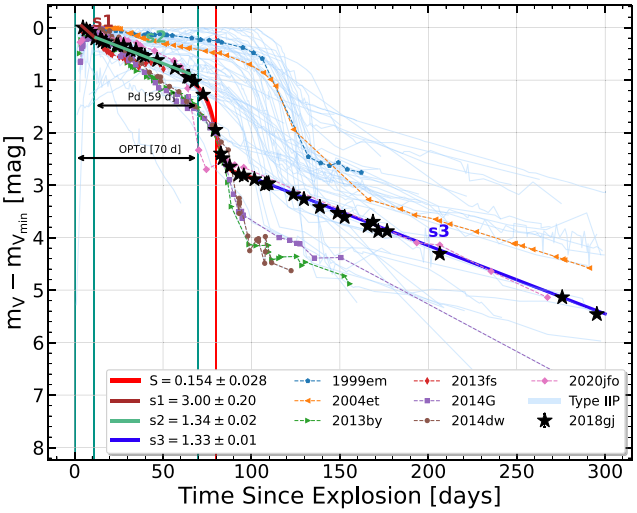

Figure 3. *V*-band light-curve evolution of SN 2018gj along with other Type II SNe. Continuous light blue lines are representative of a larger Type II sample from Anderson et al. (2014a), Faran et al. (2014a). Estimated light-curve parameters for *V*-band, viz., Optically thick phase duration (OPTd), Plateau duration (Pd), and light-curve slopes (s1, s2, and s3), are also shown. SNe data used in this plot are mentioned in Table 7.

band and, to a similar extent, in the *R* band. A similar rise is observed in the NIR *J* and *Ks* bands.

In the absence of the rising part of the *V*-band light curve, the peak absolute magnitude M_V, could not be constrained well (Figure 3). However, an upper bound on the peak $M_V \lesssim -17.0 \pm 0.1$ mag can be set. The mean of maximum M_V value for a sample of 68 Type II SNe estimated by Anderson et al. (2014a) is -16.74 ± 1.01 mag, which puts SN 2018gj toward the brighter end of Type II SNe. Furthermore, we observe a rapid decline in magnitude after +60 days, corresponding to a sharp transition from the plateau phase to the nebular phase. Using the functional form given in Elmhamdi et al. (2003a), we could find the transition time at $+79 \pm 2$ days and a plateau length (OPTd) of $\approx 70 \pm 3$ days, placing SN 2018gj in the shorter plateau group of Type IIP SNe. Following the phase definitions given in Anderson et al. (2014a), we estimated *V*-band light-curve parameters for SN 2018gj. We find s1, s2, and s3 to be 3.00 ± 0.20 mag $(100\,\mathrm{d})^{-1}$, 1.34 ± 0.02 mag $(100\,\mathrm{d})^{-1}$, and 1.33 ± 0.01 mag $(100\,\mathrm{d})^{-1}$, respectively. The *s*1 and *s*2 decline rates are quite similar to the average values obtained from the Type II sample, which are 2.65 ± 1.50 mag $(100\,\mathrm{d})^{-1}$, and 1.27 ± 0.93 mag $(100\,\mathrm{d})^{-1}$, respectively. However, the decline in *s*3 is slower than the average Type II SNe *s*3 decline rate of 1.47 ± 0.82 mag $(100\,\mathrm{d})^{-1}$.

3.4. Colors

In Figure 4, the $U-B$, $B-V$, $V-R$, and $R-I$ color evolution is shown. To compare SN 2018gj colors with other Type IIP SNe, a mean color curve from a sample of 44 Type IIP SNe, available in the literature, is created (for reference, see Table 7). We do not consider any epoch on which the number of available data points is less than five. We apply extinction correction to all the respective individual band photometry using Cardelli et al. (1989) with $R_V = 3.1$. Further, Gaussian smoothing is applied using `scipy.ndimage.Gaussian_filter1d`. The resultant mean colors, from the sample, along with 1σ scatter are overplotted with that of SN 2018gj (see Figure 4). The color evolution of SN 2018gj predominantly follows the typical Type IIP SNe behavior with slight deviations in early $U-B$, late $B-V$, and $V-R$ during the transition phase. The initial $U-B$ color (<20 days) for SN 2018gj is redder than the average $U-B$ value for Type IIP SNe whereas the $B-V$ color evolution of SN 2018gj starts to deviate after +110 days and becomes bluer than the average sample values. Further, we observe a slightly redder *elbow* kind of feature in $V-R$ mean color values around +100 days for the sample, which could signify a mean plateau length duration of 100 days for the sample. In comparison, this break in $V-R$ color evolution continuity is quite significant in SN 2018gj and is observed at +70 days, which later evolves along with the mean color evolution for the sample. The $R-I$ color evolution SN 2018gj is typical of Type IIP SNe.

3.5. Bolometric Light Curve

The multibroadband photometry is used to obtain the bolometric light curve of SN 2018gj, using the widely employed `SuperBol` (mnicholl 2018) code. The code computes pseudobolometric—bolometric curves by integrating the flux over observed bands. Further, a complete bolometric curve is estimated using blackbody extrapolations, additionally providing information about the evolution of blackbody temperature and radius. The zero-points used to convert magnitudes to fluxes are obtained from Bessell et al. (1998) for UBVRIJHK of the Johnson–Cousins–Glass system, and from Tonry et al. (2018) for the ATLAS filters. The zero-points for other filters are obtained from Spanish Virtual Observatory (SVO) Filter Profile Service (Rodrigo et al. 2012; Rodrigo & Solano 2020). To accommodate the missing epochs, the light curves were linearly interpolated, and if needed, the extrapolation was achieved using constant color with respect to the well-sampled reference band. These objectives are utilized using various tasks in `scipy`.

We estimate three different pseudobolometric—bolometric light curves. With only optical bands, a pesudobolometric light curve (L_{Opt}) is generated. Second, we include NIR data with optical and obtain Optical-Infrared (OIR) bolometric light curve (see Figure 5). As the UV data is not available throughout, we include UV data for the initial few days and estimate the bolometric light curve ($L_{UV+Opt+IR}$). We find that, using UVOIR data, the estimated bolometric light curve very closely traces the blackbody corrected estimate to the observed light curve (L_{BB}). For further analysis, we use the UVOIR observed bolometric light curve.

We missed the early detection and rise, and therefore cannot constrain the peak in any of the bands. Hence, we only report the maximum value in the pseudobolometric—bolometric light curves. For the optical bolometric light curve, the peak value obtained is $1.42 \pm 0.06 \times 10^{42}$ erg s^{-1}, and if we include the NIR and UV contributions, the values obtained are $1.84 \pm 0.06 \times 10^{42}$ and $3.18 \pm 0.08 \times 10^{42}$ erg s^{-1}, respectively. We observe that, during the initial phase of $\sim$5–15 days, the NIR contribution to the pseudobolometric light curve is only $\sim$25%. It sustains a maximum value of around $\sim$50% after the transition phase from 80 to 110 days. The NIR contribution remains significant during the nebular phase also, with an average value of $\sim 43\% \pm 2\%$, which is similar to the values estimated for other SNe (Patat et al. 2001; Elmhamdi et al. 2003a).

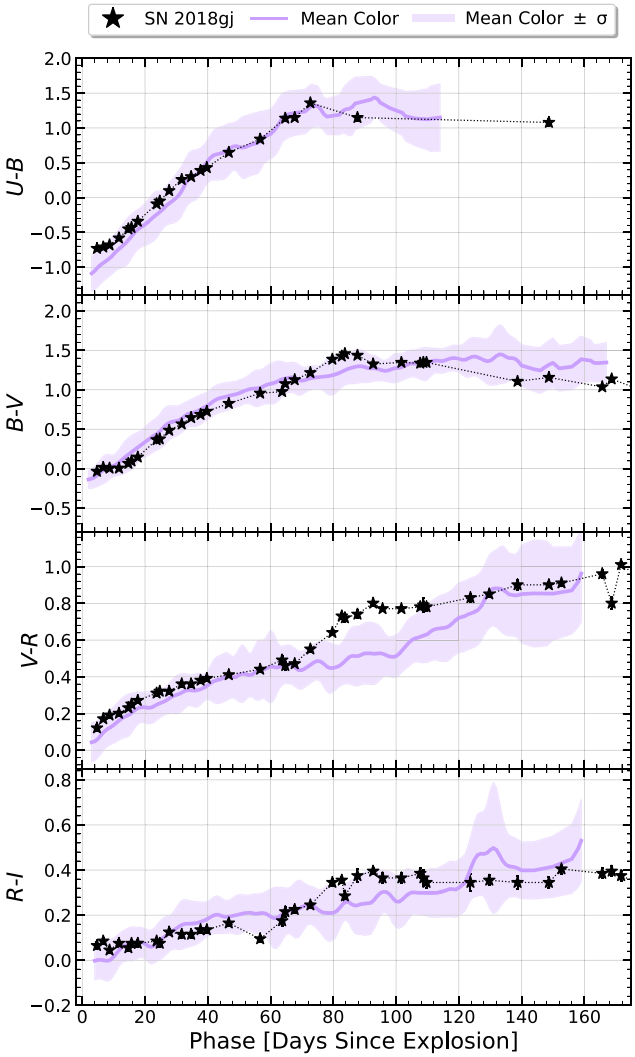

Figure 4. Mean color evolution of Type II SNe along with the color evolution of SN 2018gj for different bands is shown. The shaded region color with a solid line represents the mean colors from a larger Type IIP sample with 1σ scatter from the mean value. Sources of data have been referenced in Table 7.

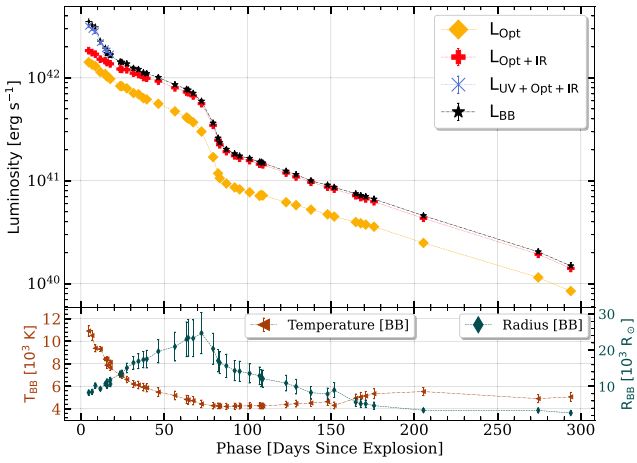

Figure 5. Pseudobolometric and bolometric light curves for SN 2018gj obtained using multiband photometry are shown. The second plot at the bottom shows the temperature and radius evolution obtained using blackbody fits from the SEDs.

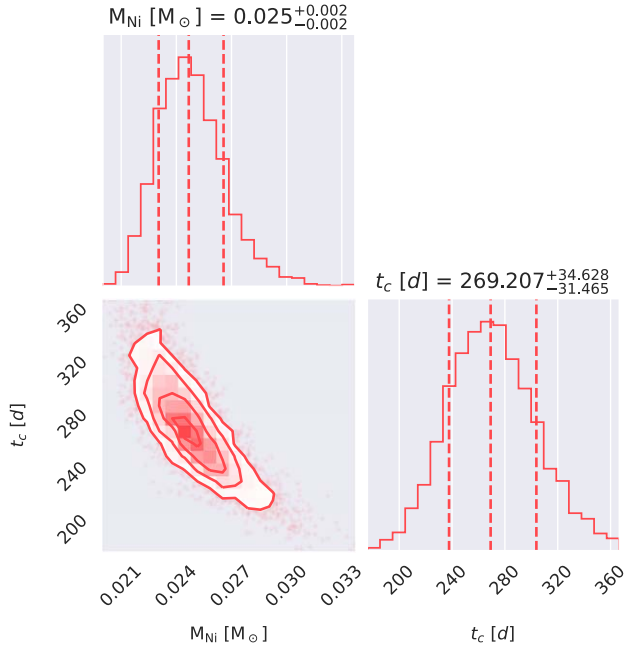

Figure 6. Posterior plot for nickel mass and characteristic time estimates for SN 2018gj using Equation (2).

3.6. Radioactive ^{56}Ni

The ^{56}Ni decay chain primarily dominates the late-time light-curve evolution of Type II SNe. It is the primary source of energy during the nebular phase of Type II SNe. We used various methods to estimate the mass of synthesized ^{56}Ni. We compared the bolometric luminosity of SN 2018gj in the nebular phase with the bolometric luminosity of SN 1987A. The mass of ^{56}Ni in SN 1987A is very well constrained using multiband photometry and hydrodynamical modeling and can be utilized to estimate the mass of ^{56}Ni in SN 2018gj. We compare the bolometric luminosity with the values obtained for SN 1987A at similar epochs and use Equation (1) to get an estimate on ^{56}Ni mass.

$$M_{\rm Ni}(\text{SN 2018gj}) \approx \mathrm{M_{Ni}(SN\ 1987A)} \times \frac{\mathrm{L}_{1987A}(\mathrm{t})}{\mathrm{L}_{2018gj}(\mathrm{t})}. \quad (1)$$

From the late time light curve (>110 days), we estimate the mass of ^{56}Ni to be $M_{\rm Ni} = 0.024 \pm 0.004\, M_{\odot}$. ^{56}Ni and characteristic timescale are also estimated using the Equation (2) and `scipy.minimize` and `emcee` packages.

$$L_{\rm obs} = L_0 \times M_{\rm Ni} \times \left[e^{-\left(\frac{t-t_0}{t_{\rm Co}}\right)} - e^{-\left(\frac{t-t_0}{t_{\rm Ni}}\right)} \right] \times \left(1 - e^{\left(-\frac{t_c^2}{(t-t_0)^2}\right)} \right). \quad (2)$$

The posterior distribution for the fits is shown in Figure 6. We obtained ^{56}Ni mass and characteristic time of $0.025 \pm 0.002\, M_{\odot}$ and 269 ± 33 days, respectively.

The steepness parameter (S) described in Elmhamdi et al. (2003a) could also be used to estimate the mass of ^{56}Ni synthesized in the explosion. Applying the refined steepness relation from Singh et al. (2018), we get a steepness parameter, $S = 0.154 \pm 0.028$, which translates to $M_{\rm Ni} = 0.028 \pm 0.005$. The estimated ^{56}Ni mass with different techniques are in good agreement with each other, with an average value of $M_{\rm Ni} = 0.026 \pm 0.007\, M_{\odot}$.

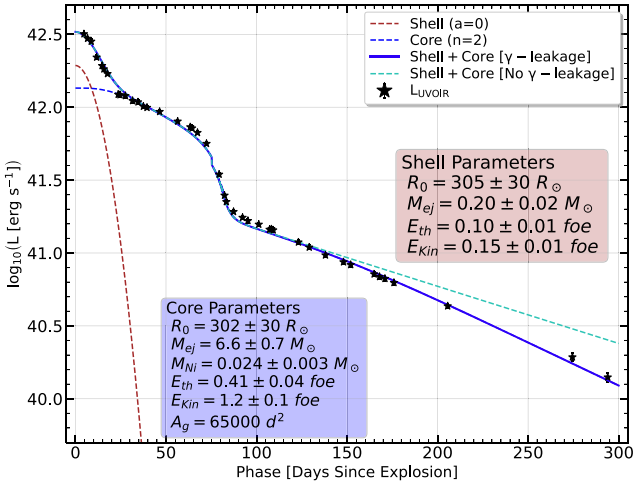

Figure 7. Semianalytical model fitting for SN 2018gj using two-component model as described in Nagy & Vinkó (2016). The contributions from the shell and the core are also shown independently. In the inset, best-fitting parameters are listed for reference. The evolution of the light curve without $\gamma-$ ray leakage is shown by the cyan dashed line.

3.7. Two-component Analytical Light-curve Model

Nagy & Vinkó (2016) formulated a two-component progenitor model to fit the observed bolometric light curves of Type IIP SNe semianalytically. This formulation is based on the seminal work by Arnett & Fu (1989) and subsequent modifications by Blinnikov & Popov (1993), Popov (1993), and Nagy et al. (2014). It could be utilized to get approximate estimates on ejecta mass ($M_{\rm ej}$), progenitor radius (R_0), total energy (E_{tot}), and synthesized ^{56}Ni mass ($M_{\rm Ni}$). The formulation divides the homologously expanding and spherically symmetric SN ejecta into two components: an inner faction with a flat (constant) density configuration; an outer region with power law or exponential density profile (Nagy et al. 2014). Both of these spherically symmetric components have different masses, radii, energies, and densities but a common center. The outer region is an extended envelope (Nagy & Vinkó 2016). Contribution to bolometric luminosity ($L_{\rm bol}$) is primarily by energy released due to recombination ($L_{\rm rec}$) and radioactive decay ($L_{\rm Ni}$) of ^{56}Ni. We use the UVOIR bolometric luminosity to approximate the semianalytical models. The best-fitting model is shown in Figure 7, and the obtained parameters are presented in Table 1. For the shell component we found, $M_{\rm ej_s} = 0.2\,M_\odot$ confined within a radius of 2.12×10^{13} cm. We find a similar radius value for the core as well ($\sim2.10\times10^{13}$ cm) with an ejecta mass, $M_{\rm ej_c} = 6.6\,M_\odot$. The outer envelope appears not far-extended, and the density is slightly higher ($\sim1.0\times10^{-8}$ g cm^{-3}) as obtained for other Type IIPs in Nagy & Vinkó (2016). For comparison, the radii obtained are between the values obtained for SN 2005cs ($R_{\rm shell} = 2.0\times10^{13}$ cm and $R_{\rm core} = 1.2\times10^{13}$ cm) and SN 2012aw ($R_{\rm shell} = 4.5\times10^{13}$ cm and $R_{\rm core} = 3.0\times10^{13}$ cm). The shell densities obtained for both the cases are 1.8×10^{-8} and 5.2×10^{-9} g cm^{-3} respectively. The values obtained for SN 2018gj are within similar ranges for other Type IIP SNe with a normal plateau duration. From the semianalytical modeling, we get a total ejecta mass, $M_{\rm ej}\approx6.8\pm0.7\,M_\odot$, radius, $R\approx305\pm30\,R_\odot$, and 1.9 ± 0.2 foe as the total energy released after the explosion.

During the nebular phase, the light-curve decline rate of SN 2018gj is 1.34 ± 0.02 mag 100 d^{-1}, much faster than 0.98 ± 0.02 mag 100 d^{-1}, the decay rate of ^{56}Co to ^{56}Fe with full $\gamma-$ ray trapping. The faster decline of the late-phase light curve indicates that the leakage of γ-rays is significant in SN 2018gj. The effect of $\gamma-$ ray leakage on the late time light curve could be introduced using the A_g parameter. This parameter is the effectiveness of $\gamma-$ ray trapping (Chatzopoulos et al. 2012); whereas, in the luminosity equation, it could be shown as $L_{\rm bol} = L_{\rm Ni}(1-\exp(-A_g/t^2)) + L_{\rm rec}$. Physically, it is related to the characteristic timescale (T_0) of the $\gamma-$ rays as $A_g = T_0^2$. The late phase light curve, powered by the radioactive decay, is fit by an $A_g = 65000$ d^2, and the mass of synthesized ^{56}Ni, $(M_{\rm Ni}) = 0.025M_\odot$. The corresponding T_0 value is 255 days, similar to the value obtained in Section 3.5. The $M_{\rm Ni}$ estimated here corroborates our previous estimates in Section 3.5. Further, the correlation between ejecta mass and opacity (correlation coefficient, r = 0.984, Nagy & Vinkó 2016) makes it insubstantial to comment on the possible progenitor mass with certainty up to 2 orders of magnitude. If we consider a proto-neutron star core of mass $\sim1.5\,M_\odot$, nominal mass loss due to winds, and the estimated ejecta mass, we could constrain the lower limit of progenitor mass, which is $\geqslant10-11\,M_\odot$, an estimate very similar to another short plateau object SN 2020jfo (Teja et al. 2022), which had a very similar light-curve shape, but a shorter plateau by $\sim$10 days.

Table 1
Parameters for Best-fitting Two-component Model

Parameters[a]	Shell	Core
Ejecta Mass, $M_{\rm ej}$ ($M_\odot$)	0.20	6.60
Radius, R (10^{13} cm)	2.12	2.10
Thermal Energy, $E_{\rm th}$ (10^{51} erg)	0.10	0.41
Kinetic Energy, $E_{\rm kin}$ (10^{51} erg)	0.15	1.2
Expansion Velocity, $v_{\rm exp}$ (1000 km s^{-1})	13.0	5.5
Opacity, κ (cm^2 g^{-1})	0.4	0.2

Note.
[a] $T_{\rm rec}\approx6000$ K, $A_g = 6500$ d^2, and $M_{\rm Ni} = 0.024\,M_\odot$.

4. Spectral Analysis

Apart from SN classification, detailed spectral studies provide insight into the ejecta composition, asymmetries, dust formation, and explosive nucleosynthesis. In this section, we present a detailed optical spectroscopic analysis of SN 2018gj. The temporal evolution of spectra is presented in Figure 8, marked with some well-identified hydrogen and metal features. The spectral sequence is not corrected for telluric absorption lines. Further, all the spectra have been scaled with photometry for absolute flux calibration and corrected for the host redshift. We study the spectral evolution spanning 31 epochs over the photospheric phase to the nebular phase beginning +5 days.

4.1. Photospheric–Plateau Phase Spectra

The early part of spectra before or around the peak for typical Type II SNe is dominated by a featureless blue continuum along with a hint of formation of broad and discrete hydrogen features, predominantly Balmer series (Hα 6563 Å, Hβ 4861 Å, Hγ 4340 Å, and Hδ 4102 Å). The features show a typical P-Cygni profile due to the expansion of the ejecta. The early spectra of SN 2018gj show these features. The He I 5876 Å appears as early as +5 days and is seen until +16 days where it gets blended with the DNa I 5890, 5896 Å. The

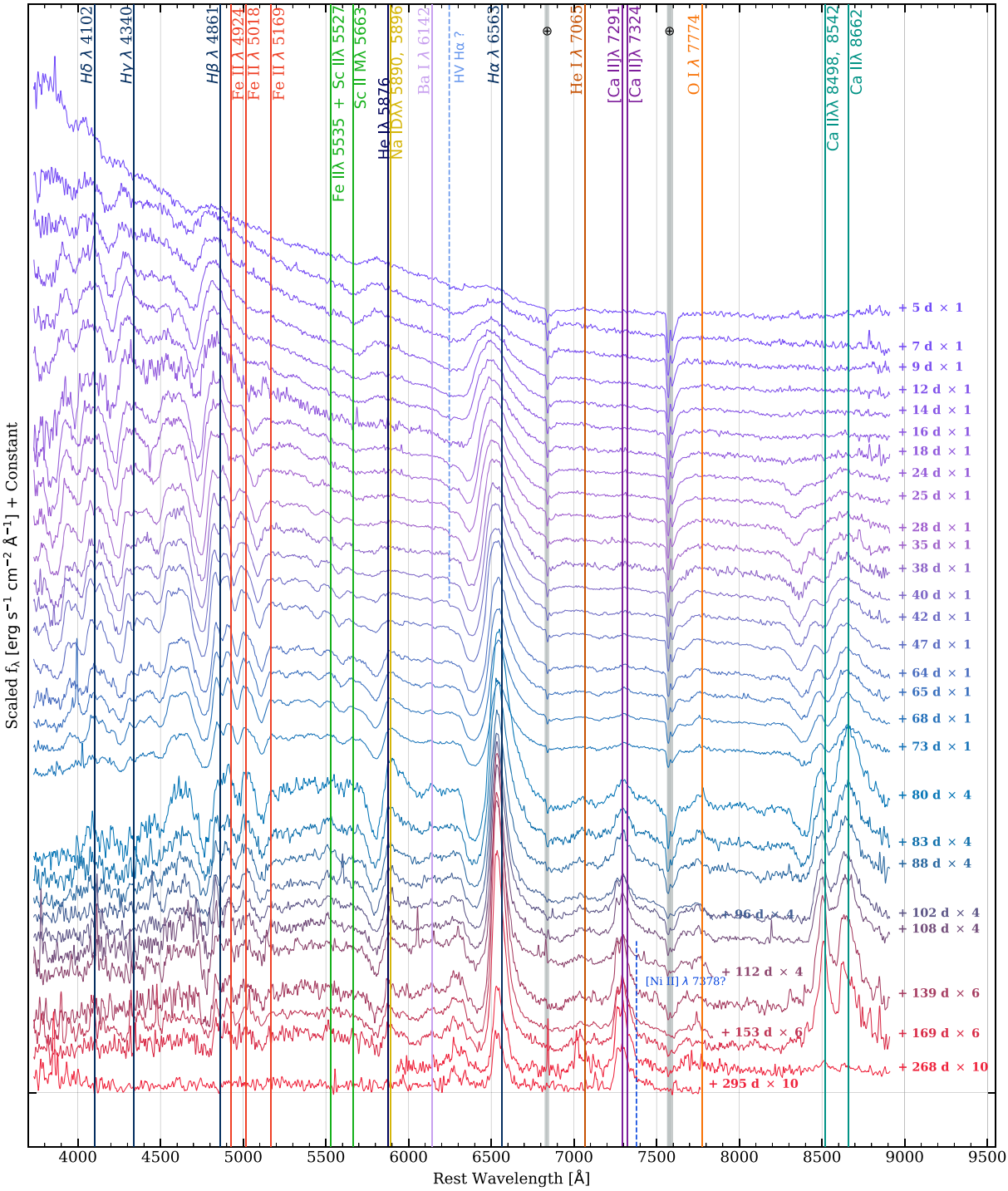

Figure 8. Spectral time series for SN 2018gj containing 31 epochs spanning 295 days post-explosion. All spectra have been calibrated with photometry for absolute flux and corrected for host redshift. Some of the prominent spectral lines have been marked for clarity.

(The data used to create this figure are available.)

temperature of the ejecta estimated using spectral energy distribution (SED; Section 3.5) around this phase is about $\gtrsim$10,000 K; as the ejecta expands, it gradually cools down. With the ejecta cooling, metallic lines are seen, dominating the blue region of the spectra. All these metallic features show well-defined P-Cygni profiles. As the SN evolves, the absorption depth increases in strength, and the Fe II multiplet 4924, 5018, 5169 Å lines are clearly seen at +24 days. The NIR region of the spectrum evolves with conspicuous Ca II triplet (8498, 8542, 8662 Å) that is visible during the same phase and becomes prominent as it evolves further. Toward the end of the plateau around $\sim +64$ days, the DNa I line develops prominently.

The spectral evolution covers the transition from the plateau phase to the nebular phase very well. We obtained four spectra during the transition period from +72 to +88 days. We find increased flux in the redder side with the increased strength of Ca II triplet. Similarly, other features become more prominent

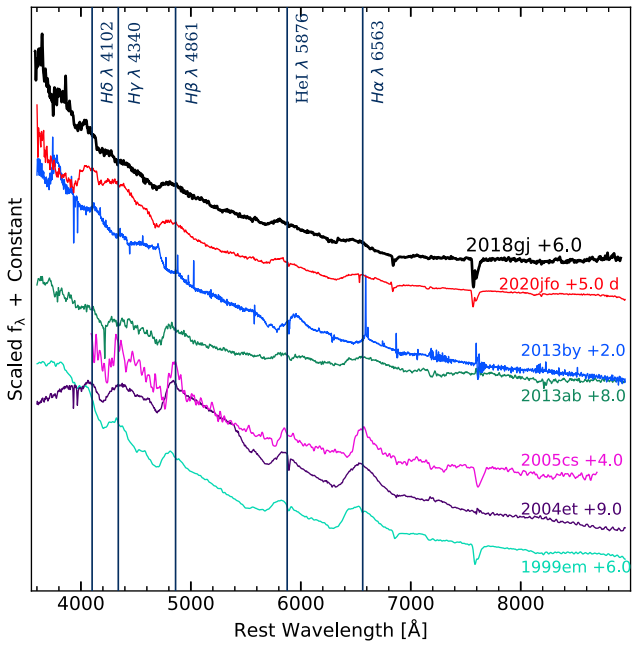

Figure 9. SN 2018gj spectrum during maximum light. Spectra of other Type II SNe around the maximum is shown for comparison. The comparison sample is drawn from Table 7.

with an increase in their strengths. Apart from the increasing strength of earlier hydrogen features, other lines, viz., Ba I 6142 Å, He I 7065 Å, and O I 7774 Å, develop and are observed clearly (Figure 8). This could be either due to the temperature change or because we can probe deep inside the ejecta as the hydrogen layer becomes transparent to the radiation from these parts. Nevertheless, from the SED fitting, we find the temperature fairly consistent within this phase. So this is primarily due to the decreased opacity of the hydrogen layer. We do not find other stark differences during the transition phase.

When we compare the spectral features of SN 2018gj with other Type II SNe, we find that these features are fairly typical and are observed in all sorts of Type II SNe whether they show plateau or decline linearly both in the early phase (Figure 9) as well as photospheric phase (Figure 10). The primary distinction is broadly the strength and spread of these features. During maximum light, the absorption trough of lines observed in SN 2018gj lies in between other SNe used for comparison. For archetypal Type IIP SNe, SN 1999em (Hamuy et al. 2001; Leonard et al. 2002a; Elmhamdi et al. 2003b) and SN 2004et (Sahu et al. 2006), we find the strength of Balmar features is more prominent around the similar phase. However, even for normal Type IIP SNe, e.g., SN 2005cs (Pastorello et al. 2006; Faran et al. 2014a) and SN 2013ab (Bose et al. 2015), the strength could vary. Although the early spectrum of SN 2020jfo (Teja et al. 2022), another short plateau event, appears very similar to the spectrum of SN 2018gj except toward the shorter wavelengths, especially around Hγ. There was the presence of ionized He in the early spectra of SN 2020jfo. Spectral comparison around mid plateau for SN 2018gj reveals the lack of metallic or fully developed features, which are more prominent in other SNe, viz., SN 2020jfo, SN 2013ej, SN 2005cs, SN 2004et, and SN 1999em. Furthermore, it is observed that the hydrogen and other metallic features in SN 2018gj are weak as compared to normal Type II SNe but similar to SN 2009kr and SN 2013ab. SN 2013ab shows many similarities with SN 2018gj around the same phase.

4.2. Ejecta Velocity

In Figure 11, we show the expansion velocities estimated using the nonblended absorption minima of various species. The absorption minimum is estimated by fitting a Gaussian profile, and the expansion velocities are measured with respect to the rest-frame wavelengths. A peculiar velocity evolution of hydrogen features is seen for the initial few days. It first rises and then declines. The rising part of the ejecta velocity has not been observed for other SNe. While the estimation of an initial lower velocity may indeed be true, the absorption features during this phase are very broad and associated with higher measurement uncertainty. A shallow absorption feature is seen around 6200 Å during the early phases (until ∼40 days). It could be attributed to an HV Hα feature (Dessart & Hillier 2022), at a velocity of ∼15,000 km s^{-1}. Figure 11 also shows a comparison of the SN 2018gj velocities with the mean expansion velocities obtained from a large sample of Type II SNe (Gutiérrez et al. 2017). The expansion velocities for SN 2018gj are toward the higher end of 1σ scatter from the mean. It continues to follow this higher-velocity trend even after transitioning from the plateau phase to the nebular phase. The expansion velocity inferred from Fe II features is found to be higher than the mean value initially; however, later, it follows a trend similar to the mean of the sample.

From various absorption features, we estimate that the layers of the ejecta are moving with velocities higher than 10,000 km s^{-1}. Although the temperature around a similar phase estimated for SN 1999em is similar to SN 2018gj, the Hα velocity inferred was much higher (∼16,000 km s^{-1}) (Elmhamdi et al. 2003b). In the case of SN 2013ej (Valenti et al. 2014) and SN 2020jfo, the expansion velocities are around 13,000 km s^{-1} and comparable to that of SN 2018gj. As the ejecta evolves with time, it starts to slow down (<9000 km s^{-1} around +20 days) and cool to a lower temperature (⩽8000 K around +20 days).

During the photospheric phase, the expansion velocities continue to follow the declining trend and reach ∼8000 km s^{-1} around +40 days. Afterwards, the decline is very slow and does not follow the average trend. The expansion velocities estimated using hydrogen features are on the higher side for the Type II SNe. For SN 1999em around +40 days, typical temperatures are 5000–6000 K and Hα velocity of about 6000 km s^{-1} (Elmhamdi et al. 2003b). In 2005cs velocities are much lower around +40 days and are estimated as ⩽4000 and 2000 km s^{-1} for Hα and metal lines, respectively (Pastorello et al. 2006). Around similar phases, Hα and metal velocities for SN 2004et are 7500 and 4500 km s^{-1}, respectively. In the cases of SN 2009kr, SN 2013by, and SN 2020jfo, Hα velocities are ⩽7000 km s^{-1} whereas for SN 2018gj it is close to the velocities estimated for SN 2013ab (8000 km s^{-1}) and SN 2013ej (8500 km s^{-1}).

Similar observations are true for velocities estimated using metal lines. Typical expansion velocities around the plateau phase start at 6000 km s^{-1} and slow down to ∼3000 km s^{-1} toward the end of the plateau phase.

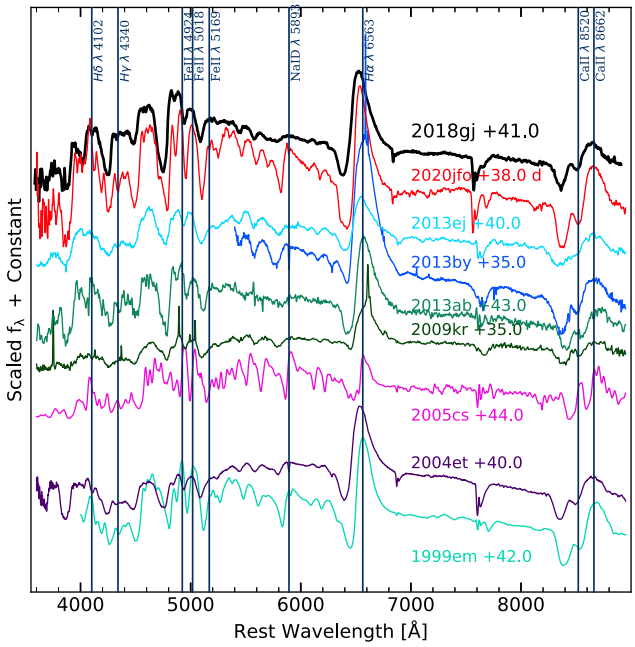

Figure 10. Spectrum of SN 2018gj during plateau phase is shown in comparison with other Type II SNe. The comparison sample is drawn from Table 7.

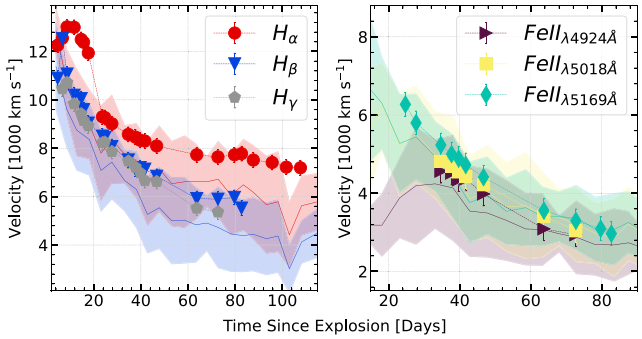

Figure 11. Temporal velocity evolution of various lines identified in the spectra using the absorption minimum is shown here. The velocities have been compared with the sample from Gutiérrez et al. (2017) where the solid lines are the mean values from the sample, and the shaded area around it in similar color represents the 1σ scatter from the mean velocities.

4.3. Nebular Phase Spectra

When the receding photosphere reaches the base of the outer envelope, the plateau—photospheric phase ends, and the SN transitions to the nebular phase. The continuous expansion reduces temperature, column density, and optical depth (Jerkstrand 2017a). The ejecta is optically thin, and the inner ejecta layers are probed. SN in this phase is still optically bright, and the prominent energy source is the radioactive decay chain of ^{56}Ni synthesized in the explosion. The midpoint of transition happens around +80 days, and several metal lines originating from forbidden transitions, e.g., [Ca II] 7291, 7324 Å start appearing. The strength of Na ID 5893 Å and Ca I triplet keeps on increasing as the ejecta evolves with time. Other forbidden lines, viz., [Fe II] 6118, 7155, 7172 Å, [O I] 6300, 6364 Å, also start to appear in the spectra. Blueward of Ca triplet, we identify the O I 7774 Å. The presence of Hα continues during the nebular phase and is the dominant line in the spectrum, although much narrower.

Figure 12 shows the comparison of nebular phase spectra for SN 2018gj with several other Type II SNe. The O I 7774 Å line in SN 2018gj is found to be weakest in comparison to other Type II SNe except for SN 2013by. Apart from certain features common in Type II SNe, we find a hint of stable [Ni II] 7378 Å with emission feature having an intrinsic velocity similar to other emission features starting from +112 days (Figure 8). This feature was observed in SN 2020jfo ∼+196 days as presented in Teja et al. (2022). However, it is quite possible that, in SN 2020jfo, the stable Ni was present from an earlier epoch, but due to its proximity to the Sun, the first nebular spectrum could be obtained ∼+196 days. This feature is very prominent in SN 2020jfo but weak in SN 2018gj.

4.4. Blueshifted Emission from Photospheric Phase to Nebular Phase

We observed blueshift in the emission peaks in the spectral evolution of SN 2018gj. In Figure 13, the region around Hα has been plotted, showcasing this persistent blueshift in the Hα emission peak. The Hα emission peak is shifted by $\sim 4500\,\mathrm{km\,s^{-1}}$ around +10 days, which decreases monotonically until the end of the plateau around +75 days where it reaches a value $\sim 500\,\mathrm{km\,s^{-1}}$ but never reaches rest wavelengths (Figure 14). Instead, we observed the shift to increase during the transition phase and settle on a value of $-1000\,\mathrm{km\,s^{-1}}$. The blueshift is seen until the last available spectrum (+295 d). The shift is not only observed in the Hα but also seen in other lines with similar values.

4.5. Progenitor Mass Estimates Using Nebular Lines

In addition to light-curve modeling, there are other independent methods for determining the progenitor's mass. One such approach is to utilize the nebular phase spectra, which can provide insight into the metallic lines that arise from stellar nucleosynthesis. Jerkstrand et al. (2014) demonstrated that the late-phase lines of [O I] 6300, 6364 Å and [Ca II] 7291, 7324 Å can serve as proxies for progenitor mass. To constrain the progenitor mass of SN 2018gj, we compared the nebular phase spectrum at +295 days with model spectra from Jerkstrand (2017b). The model spectra for progenitor masses of 12, 15, 19, and 25 $M_\odot$ have been scaled for the ^{56}Ni mass and the distance of SN 2018gj (in contrast to 5.5 Mpc for the model spectra) (Figure 15). To account for the difference in phase between the model spectra and the observed spectrum, the observed spectrum was scaled by the brightness difference due to dissimilarity in phases determined from the characteristic timescale (t_c) obtained from the ^{56}Ni-decay-powered phase of the light curve using $f_{corr} = f_{\rm obs}/(1 - e^{-(t_c/phase)})$ (Singh et al. 2019).

The comparison of [O I] 6300 Å, 6364 Å line fluxes of the observed spectra with the spectral models suggests a progenitor of mass $\leqslant 15\,M_\odot$. However, the observed Hα flux is relatively weak as compared to the $15\,M_\odot$ progenitor, indicating a partially stripped hydrogen envelope in SN 2018gj. In CCSNe, the mass of calcium synthesized in the explosion is insensitive to the progenitor's zero-age main-sequence mass, whereas the mass of synthesized oxygen depends on it. Hence, the [Ca II] / [O I] flux ratio is a useful indicator of the progenitor mass (Fransson & Chevalier 1989). The lower the value of the ratio, the heavier the progenitor. As seen in the model spectra presented in Figure 15, the [Ca II] 7291, 7324 Å lines from

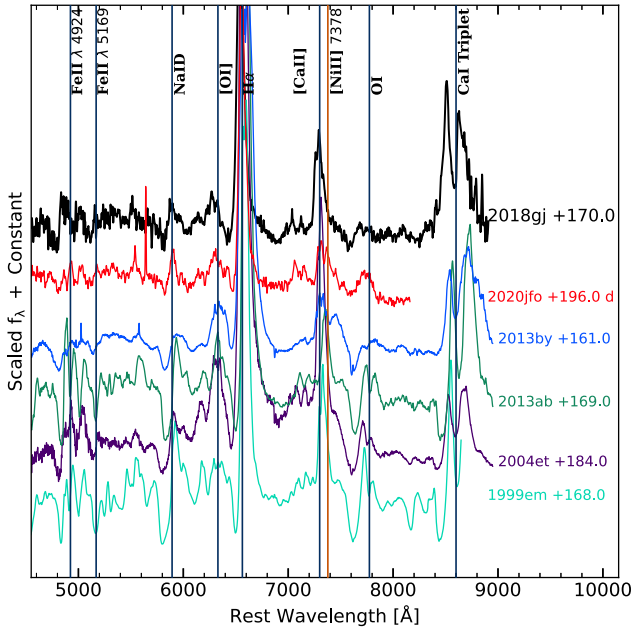

Figure 12. Spectral comparison of SN 2018gj with other Type II SNe around similar epochs during the nebular phase.

different mass models have similar line strength whereas it is differentiable in the case of [O I] 6300, 6364 Å and increases with the progenitor masses. In the case of SN 2018gj, the [Ca II] lines are stronger than those from the model spectra, whereas [O I] lines are much weaker. Therefore, the [Ca II] / [O I] line flux ratio is much larger than one indicating a low-mass progenitor.

5. Hydrodynamical Modeling

The lower bound for progenitor mass obtained using the semianalytical light-curve modeling and the independent progenitor mass estimated using the nebular spectrum comparison with model spectra suggests that SN 2018gj resulted from a low-mass RSG progenitor with zero-age-main-sequence (ZAMS) mass ranging from 10–15 $M_{\odot}$. Model light curves of normal Type IIP SNe have been extensively studied (Dessart et al. 2010; Sukhbold et al. 2016; Eldridge et al. 2018), and in some cases, refined analytical equations are provided to get estimates on the progenitor properties (Goldberg et al. 2019). We compare the observables obtained for SN 2018gj with the analytical equations (Goldberg et al. 2019) obtained for Type IIP and find that, for a specific radius range of RSG ($300 - 1200\,R_{\odot}$), the equations hint at a shallow ejecta mass ($0.5 - 2.5\,M_{\odot}$) and explosion energy ($0.4 - 0.03$ foe; see Appendix C). These ejecta masses are in disagreement with our previous estimates obtained using semianalytical modeling and nebular spectra comparisons. Even if we use radii obtained from the semianalytical modeling in the scaling relation, the values obtained for the ejecta mass and explosion energy are not similar to those obtained from the semianalytical modeling. But as we go for much smaller radii ($\sim$200 $R_{\odot}$), the ejecta mass (4.5 $M_{\odot}$) and explosion energy ($\sim$ 1 foe) increase reaching closer to the values obtained using semianalytical modeling. However, it is noted here that the analytical equations are calibrated for the SNe IIP that show a normal plateau of $\sim$100 days and may not necessarily be valid for short plateaus as also indicated by Hiramatsu et al. (2021).

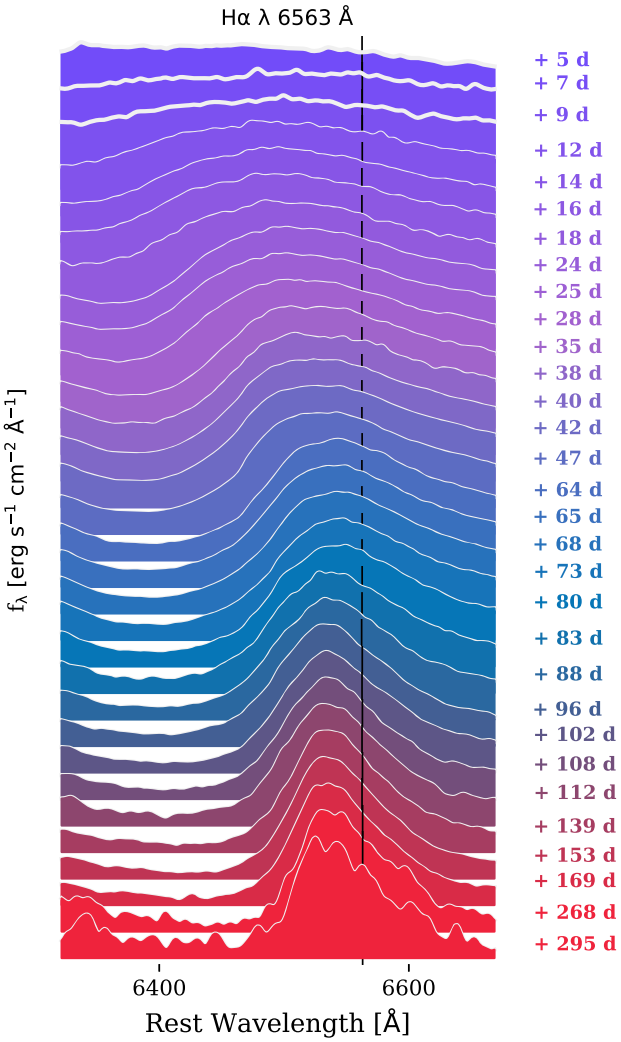

Figure 13. Focused view of spectral time series for Hα line in SN 2018gj. The black line marked is the rest wavelength for Hα. The spectra are corrected for host redshift, and it is evident that the peak of emission features never reaches the rest wavelength.

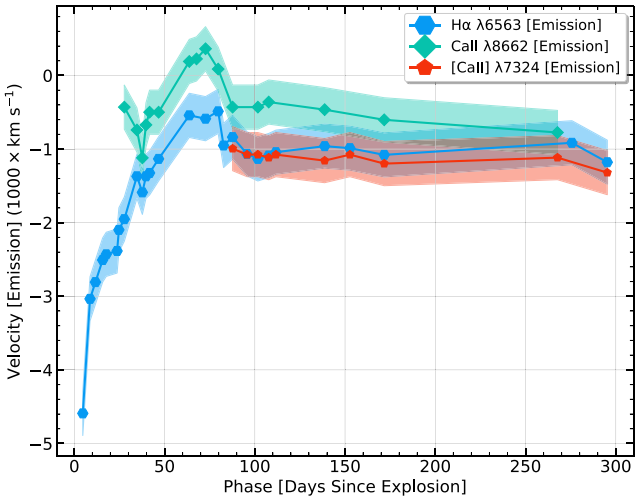

Figure 14. Velocity evolution of blueshifted Hα emission peak. Velocity evolution for emission features obtained using other ions has also been plotted.

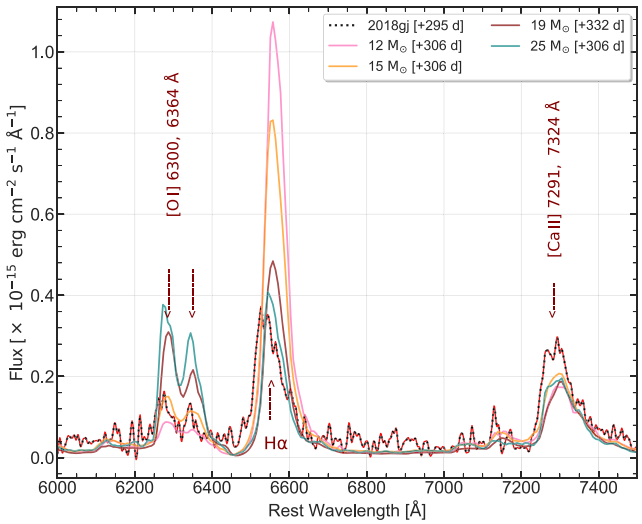

Figure 15. Late phase (+295 days) spectrum of SN 2018gj compared with the model spectra around similar phase to estimate the initial mass of the progenitor. The model spectra are obtained from Jerkstrand (2017b).

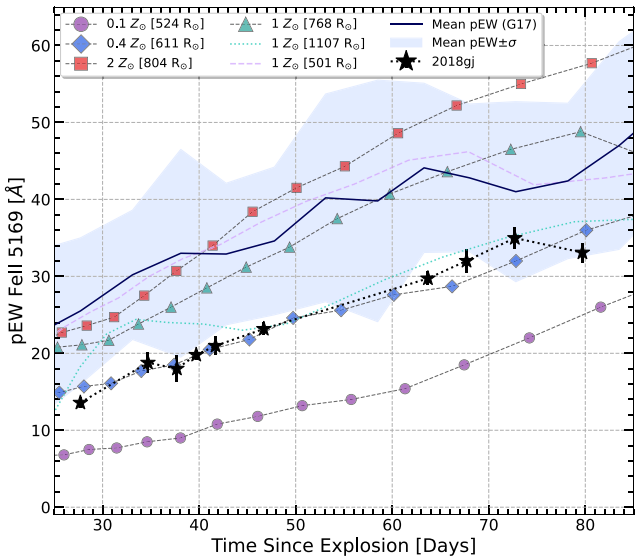

Figure 16. Temporal evolution of pseudo-equivalent width (pEW) for Fe II 5169 Å line obtained using optical spectra. Other markers represent the pEWs obtained from models given in Dessart et al. (2013). The solid blue line and the shaded region around it represent the mean pEW and the corresponding 1σ scatter about the mean for a larger sample of Type II SNe given in Gutiérrez et al. (2017).

A more robust way forward is to perform a complete hydrodynamical modeling to better understand the progenitor, its evolution history, and other SN explosion parameters. We perform the modeling using the Modules for Experiments in Stellar Astrophysics (MESA version r-15140; Paxton et al. 2011, 2013, 2015, 2018, 2019) and STELLA (Blinnikov & Sorokina 2004; Baklanov et al. 2005; Blinnikov et al. 2006) packaged within MESA. It was compiled using MESA SDK (Software Development Kit) (version x86_64-linux-20.12.1; Townsend 2020). The modeling setup follows the values prescribed in Farmer et al. (2016). In lower-mass models, we had increased the *max_model_number* in each *inlists* to accommodate longer evolution times. We fixed the overshooting values to default settings ($f = 0.01$, $f_0 = 0.005$). We set the *varcontrol_target* $= 10^{-4}$ for the convergence of models with higher mass loss. Some other basic setup parameters are as follows: the nuclear reaction rates network used "approx21_cr60_plus_co56.net," provided within MESA. These rates are primarily from the Nuclear Astrophysics Compilation of Reaction rates (Angulo 1999), and the Joint Institute for Nuclear Astrophysics, JINA reaction rates (REACLIB; Cyburt et al. 2010). The mixing length parameter (MLT_option) defaults to *Henyey* (Henyey et al. 1965), with $\alpha_{MLT} = 1.5 - 2.0$, where α_{MLT} is the ratio of mixing length to the pressure scale height (=P/gρ). Other than the models with $19\,M_\odot$ and $13\,M_\odot$ ($\alpha_{dutch} = 3.0$) where α_{MLT} is set to default value of 1.5, we set it to 2.0 for the remaining models. Cool and hot wind schemes (α_{dutch}) for the red giant branch or asymptotic giant branch phase are considered *Dutch*, combining works by many Dutch authors. The primary combination chosen is based on the work by Glebbeek et al. (2009). Typically, if the surface H has a mass fraction < 0.4 and a $T_{\rm eff} > 10^4$ K, the scheme used is from Vink et al. (2001); otherwise, it is from Nugis & Lamers (2000). The default *Ledoux* criterion is used to determine the position of the convective boundaries.

The light-curve modeling in MESA+STELLA was achieved in the three broad steps: i) progenitor evolution, ii) synthetic explosion, shock propagation, shock breakout, and iii) ejecta evolution. In the first step, we used "make_pre_ccsnIIp" example provided in *test suites* to evolve a pre-main-sequence star until the development of the iron core further leading to its rapid infall. Given that there is no solution to achieve a spontaneous explosion in MESA, the *test suite*, namely "ccsnIIp", provides an alternative methodology to achieve the desired explosion. Primarily, a thin layer (mass $\sim$0.01 $M_\odot$) at the inner boundary is injected with a tremendous amount of energy over a brief period (5 ms) to achieve the synthetic explosion. Finally, the shock is propagated with various layers, and the structure and hydrodynamical parameters are obtained just before the shock breakout as input to the STELLA (Paxton et al. 2018). Further details of the steps adopted and the parameters adjusted from evolution to explosion and handover to STELLA could be obtained from Farmer et al. (2016), Teja et al. (2022). We used 400 zones for STELLA with 40 extra zones in case of CSM. For the case of bolometric light curves, we used 40 frequency bins. However, in the case of UBVRI light curves, we had estimated $13M_\odot$ cases for 120 frequency bins for better resolution. Another parameter crucial in modeling is the metallicity, which could affect wind-driven mass losses, the mass of the hydrogen envelope, and the line-profile signatures in Type II SNe (Dessart et al. 2013). Metallicity becomes more significant in the case of short plateaus due to extensive wind mass losses and smaller hydrogen envelopes. Since SN 2018gj is far from its host galaxy center, we tried to image the region around the SN in search of possible nearby H II using a narrowband Hα filter. Unfortunately, we could not detect any such region for sufficiently long exposures. To crudely estimate metallicity, we utilized the pEW evolution of Fe II λ5169 Å. We compared it with the models presented in Dessart et al. (2013). Figure 16 shows the time evolution of pEW of Fe II λ5169 Å along with the models presented in Dessart et al. (2013). It also shows the mean and 1σ scatter in corresponding values for a larger Type II SNe sample (Gutiérrez et al. 2017). From these models, we found that two models with $0.5\,Z_\odot$ and $Z_\odot$ matched with the

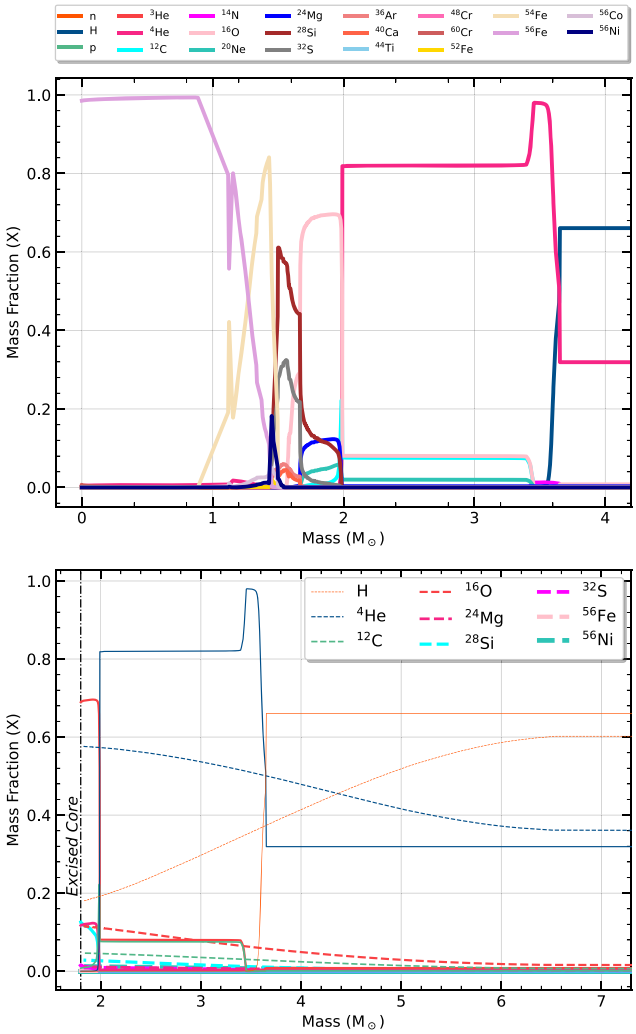

Figure 17. Top: 1D representation of mass fractions for 13 $M_{\odot}$ ZAMS model with final mass 7.3 $M_{\odot}$. The elements are part of the nuclear reaction rates network used in the model's evolution. The abscissa is shown until 4 $M_{\odot}$ as the trend followed beyond it is the same for the outer hydrogen envelope. Bottom: the effect of mixing with the implementation of Duffell RTI on the ejecta structure just before the breakout is shown for some of the prominent elements for the same model as in the top panel.

pEW obtained in the case of SN 2018gj. Hence, we fix the metallicity of all the models to be of solar values.

We tried to evolve progenitors with ZAMS masses 13 $M_{\odot}$ and 14 $M_{\odot}$ and extracted their pseudobolometric—bolometric light-curve evolution after they explode. We checked for higher-mass models also (see Appendix D). We found out that, with standard mass loss by winds, none of the models was able to reproduce a short plateau. In most cases, the plateau duration was typical of normal Type IIP SNe. However, we could get shorter plateaus as we enhanced the mass-loss rate through winds using the *wind scaling factor*, $\alpha_{dutch} = 3.0$–5.5. As the plateau duration primarily depends on the hydrogen envelope mass, achieving shorter plateaus from each of these progenitor masses with the correct mass loss was possible. However, the simultaneous match to the expansion velocities was not achieved in the models for 14 $M_{\odot}$ progenitors. In the case of 13 $M_{\odot}$ models, we were able to match the light curve and expansion velocities up to the initial 50 days. Figure 17 gives the final composition for one of the 13 $M_{\odot}$ models representing the elements used in the progenitor structure. It also shows the mixing effect on the ejecta composition with the implementation of Duffell Rayleigh-Taylor instabilities (RTI) in MESA (Duffell 2016). The mass fractions beyond 4 $M_{\odot}$ are very similar with no recognizable changes and, therefore, are not shown in the top panel of Figure 17. Although elements are mixed at different mass coordinates, the core and outer structure fairly consist of iron and hydrogen, respectively. From the current understanding of single-star evolution, high-mass RSG (>20 $M_{\odot}$), with enough mass loss, could give a smaller plateau as obtained in the works by Dessart et al. (2010), Hiramatsu et al. (2021). To explore the possibility of a high-mass progenitor, we also attempted to generate models using 19 $M_{\odot}$ progenitors, as this is the upper limit for directly detected progenitors. It is possible to obtain smaller plateau lengths with lower mass-loss rates, but these models failed to reproduce the velocity evolution of the ejecta [Appendix D]. Properties of some of the pre-SN progenitors are provided in Table 2, giving details of the initial and final masses of the progenitors.

Further, masses of helium and iron core present during evolution are also mentioned in the table. In addition to the used parameters, Table 2 also lists the various properties of the pre-SN star, viz., effective temperature, luminosity, age, and radius. We only show those models where we could achieve smaller plateau lengths. Detailed descriptions and analyses of these individual models are beyond the scope of this work. As expected from the initial mass of the progenitor models, there are not many differences in the pre-SN structure apart from the mass difference of the hydrogen envelope. All the models with the same initial mass have similar evolution times, effective temperatures, core masses, and luminosities.

We attempted to generate the model light curves to match the observed UVOIR bolometric luminosity. After achieving a desired plateau length in the model light curves, the mass of synthesized nickel and explosion energy were constrained by varying the nickel mass (*x_ctrl*(12)) and explosion energy (*inject_until_reach_model_with_total_energy*) parameters during the explosion and shock propagation. Figure 18 shows all the models for 13 $M_{\odot}$ with plateau lengths 80 ± 10 days. The bolometric luminosity of SN 2018gj is overplotted. In the model, the explosion energy and nickel mass are well constrained; however, the initial peak (s1) is slightly underluminous. Instead of comparing the bolometric luminosity, we compare the observed pseudo (optical) bolometric luminosity with modeled pseudobolometric luminosity (L_{UBVRI}), which reveals the underluminous (s1) phase more prominently. We discuss the possible presence of CSM interaction in the subsequent section. The nickel mass obtained with the hydrodynamical modeling corroborates the earlier mass estimates through various techniques. The explosion energy obtained is slightly less than the semianalytical modeling estimates.

6. Discussion

6.1. Blueshifted Emission

As described earlier in Section 4.4, we observed the emission peaks were blueshifted, and these shifts were observed until the late phase. The blueshifted emission during the photospheric phase has been observed and discussed explicitly in many works (Andrews et al. 2011; Bose et al. 2015; Dastidar et al. 2018). It has been established in Anderson et al. (2014b) that this feature

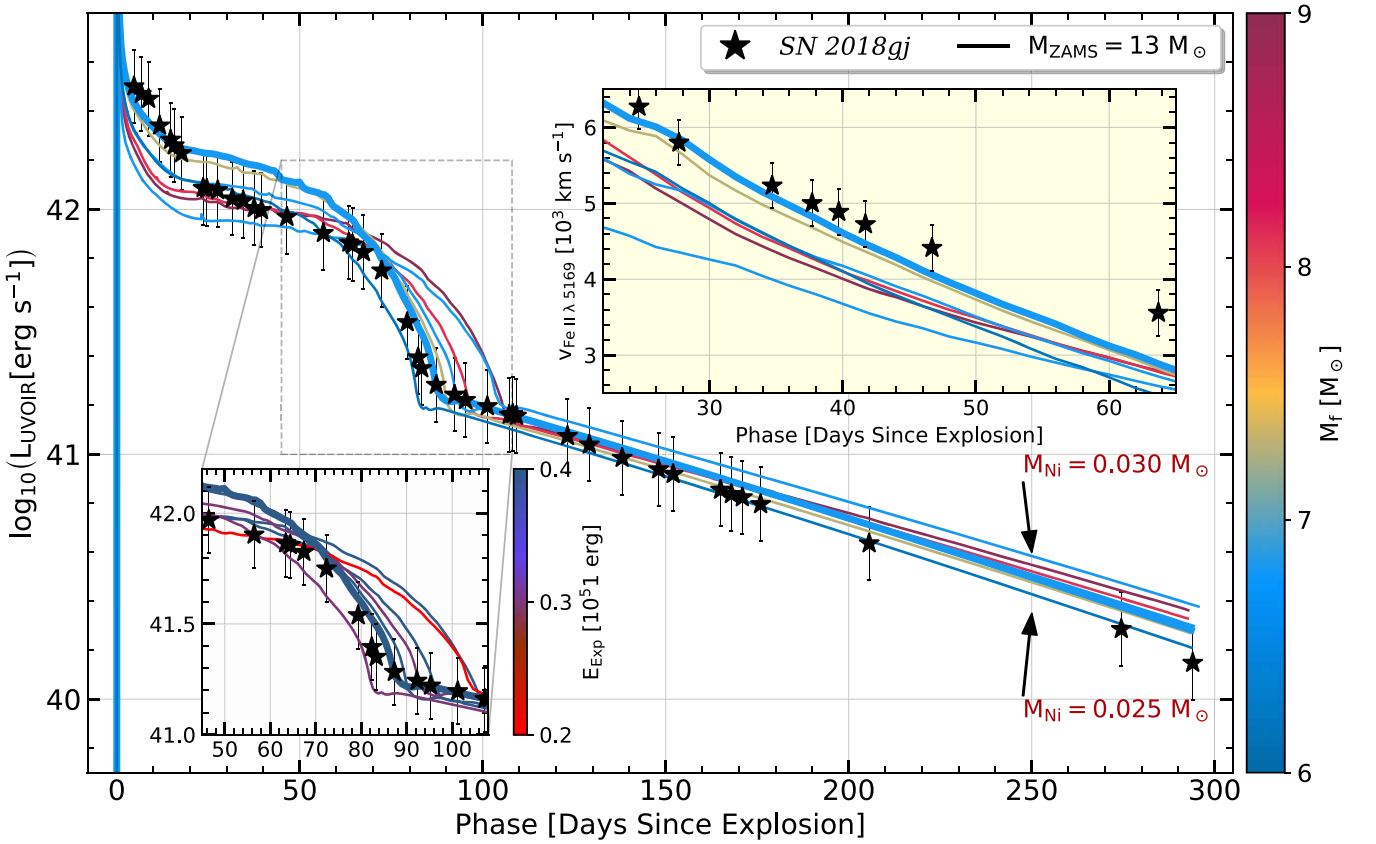

Figure 18. Variations in 13 $M_{\odot}$ ZAMS model using different parameters to achieve a shorter plateau length. Zoomed out, a plot in the bottom left shows the variation in explosion energy for different model light curves around the plateau transition. The second plot in the right inset shows the corresponding Fe 5169 velocities obtained using models. The thicker line represents the model where the expansion velocity could be matched with the observed velocities.

Table 2
Parameters for Pre-SN–Explosion Progenitor Models Evolved from MESA That Were Used to Generate Model Light Curves in STELLA

Pre-Supernova Parameters										Explosion Parameters	
M_i ($M_{\odot}$)	α_{Dutch}	M_f ($M_{\odot}$)	$M_{\rm H-rich}$ ($M_{\odot}$)	$M_{He-core}$ ($M_{\odot}$)	$M_{\rm Fe-core}$ ($M_{\odot}$)	logT$_{\rm eff}$ T$_{\rm eff}$(K)	logL L(erg s^{-1})	Age (Myr)	Radius ($R_{\odot}$)	E_{Exp} (10^{51} erg)	$M_{\rm Ni}$ ($M_{\odot}$)
13	3.0	9.1	5.35	3.75	1.50	3.57	4.83	16.7	620	0.4	0.025
	4.0	8.2	4.54	3.63	1.53	3.57	4.80	16.7	609	0.4	0.025
	4.5	7.3	3.66	3.65	1.48	3.51	4.77	16.7	773	0.4	0.030
	5.0	6.9	3.26	3.60	1.52	3.51	4.80	16.8	794	0.2	0.027
	5.0	6.9	3.26	3.60	1.52	3.51	4.80	16.8	794	0.3	0.027
	5.0	**6.9**	**3.26**	**3.60**	**1.52**	**3.51**	**4.80**	**16.8**	**794**	**0.4**	**0.028**
	5.5	6.3	2.69	3.57	1.61	3.52	4.72	16.9	705	0.3	0.025

Note. The values in bold represent the best-fit model.

is typical to Type IIP SNe during the early–photospheric phase. It was concluded by Chugai (1988) that these blueshifted emission peaks during the photospheric phase are due to the diffuse reflection of the photosphere's resonance radiation. Primarily in all the cases, the shifts are only present up to the late photospheric phase or early nebular phase except in the case of SN 2007it (Andrews et al. 2011) where it has been observed until 150 days post-explosion. Anderson et al. (2014b) utilizing the Type IIP modeled spectra from Dessart et al. (2013) showed the shifts in emission peaks vanish after photospheric phase, and the emission peaks are observed at rest wavelengths. Interestingly, the shifted peak is reported for Hα and not any other lines.

The blueshift in the emission peaks observed in the spectral evolution of SN 2018gj is a typical feature for Type IIP SNe during the photospheric phase. But the intriguing aspect is the presence of these shifts until the late nebular phase is not just limited to the prominent Hα feature. Observance of such shifts during the late nebular phase is rare in most of the usual Type IIP SNe studied in the literature. The blueward shift might not be physical but apparent and can be explained from the argument presented in Anderson et al. (2014b) regarding ejecta geometry and its composition. One of the critical factors is the changes in the opacity values. Opacity within the photosphere and above depends on various physical processes, viz., density, composition, and degree of ionization within the ejecta

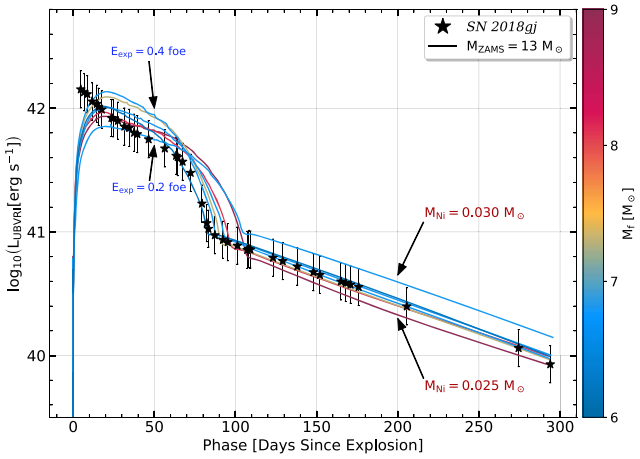

Figure 19. Optical bolometric luminosities obtained using MESA+STELLA are plotted along with the optical bolometric light curve of SN 2018gj. The initial rise is not fitting well in the optical regime.

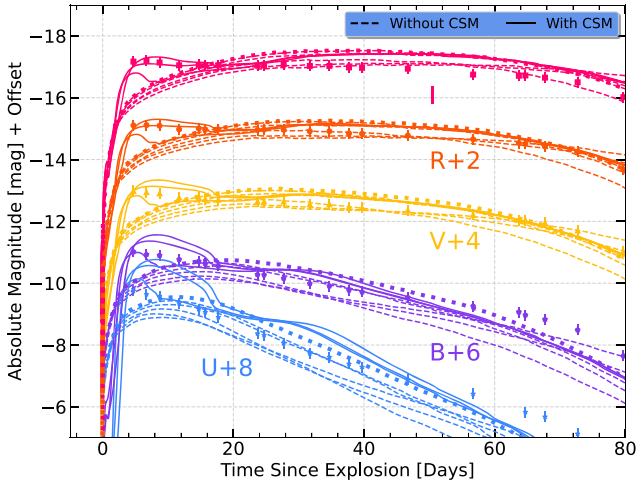

Figure 20. The effect of adding CSM around the progenitor is prominently seen in the early stage and can explain the initial excess in the individual light curves in redder bands. The thicker dashed lines represent the light curves obtained using 120 frequency bins.

(Sim 2017). During the photospheric phase, the density structure in Type IIP ejecta is much steeper. It enhances the confinement of the emission and/or absorption line. Further, it aggravates the concealment of the receding portion of the ejecta, hence biasing the blueward line emission for a distant observer during photospheric phase (Anderson et al. 2014b).

But the above reasoning might not be valid during the nebular phase when the ejecta behaves like an emission line nebulae. Other radiative transfer effects might come into play, especially due to free electrons, photoionization, or the presence of dust (Jerkstrand 2017a). During the nebular phase, the amount of electron scattering is relatively low, with an optical depth of $\tau_e \leqslant 1$. Most photons will not be scattered or will only be scattered once. As a result, the distortions in the line profile are not significant (Jerkstrand 2017a). However, the scattering does cause a slight blueshift of the peak. For instance, when $\tau_e = 1$, the shift is approximately $\Delta\lambda/\lambda_0(V_{\rm max}/c) = -0.13$, which corresponds to a velocity shift of 390 km s^{-1} for a line that is 3000 km s^{-1} wide (Jerkstrand 2017a). The blueshift observed in the spectra is much larger than the values obtained for typical opacity. Hence, this might not be the cause of the observed shifts.

The continuous absorptive opacity or the photon destruction (continuous absorption) by dust or photoionization could also cause a significant blueshift. For $\tau_e = 1$, the shift is approximately $\Delta\lambda/\lambda_0(V_{\rm max}/c) = -0.31$, which corresponds to a velocity shift of $\approx$900 km s^{-1} (Jerkstrand 2017a), which is significant and close to the observed values. But for these effects, the presence of dust or enough optically thick material is required. As a considerable fraction of the hydrogen envelope is removed from the progenitor of SN 2018gj, the presence of optically thick material also does not seem plausible. However, the presence of pre-existing dust or early dust formation in the ejecta could be a possibility. We do not find a convincing signature for the presence of dust in the ejecta. During the nebular phase, the light curve in the optical band is found to decline faster than the ^{56}Co decay rate, which could be due to the light absorption by dust. In such a scenario, due to reprocessing of light by the dust particles, the light-curve decline in the redder bands is expected to be slower. However, on the contrary, in SN 2018gj, the light curves in the redder bands are found to decline much faster (Section 3.2).

Since the SN occurred in the outskirts of the host galaxy, the intrinsically HV of the progenitor star toward the line of sight could also be a possibility. Though, it is rare to find such high-mass hyper-velocity stars going rogue but could be possible, as observed in Evans & Massey (2015).

6.2. CSM Interaction?

A piece of substantial evidence has been found in favor of early CSM interaction having a signature in the light curves. However, we do not see any interaction feature in the spectral evolution. When we try to fit pseudo bolometric luminosity with UBVRI bolometric luminosity from the models (see Figure 19), we could see that the initial part does not fit that well until we introduce CSM interaction (see Figure 20).

In Figure 20, we introduce three CSM profiles with different wind evolution time and mass-loss rates giving total masses 0.1, 0.15, 0.20 $M_\odot$ with different extents. We observe that the initial light evolution could be explained with less than 0.15 $M_\odot$ of CSM, which is close to the progenitor. The enhanced pre-SN wind was activated 10–20 yr before the explosion.

There is no evidence in spectra to corroborate the presence of CSM around the progenitor. Either the lack of CSM interaction evidence in spectra is due to some nonspherical geometry, or it might be the intrinsic feature of these SNe and warrant a further understanding of these light-curve rise times.

7. Conclusion

In this work, we presented a detailed investigation of a short plateau Type II SN, SN 2018gj, which exhibited a plateau lasting for $\sim$70 days in its light curve. This plateau duration is significantly less than the characteristic plateau length of $\sim$100 days for Type IIP SNe. We carried out detailed photometric observations in UV, optical, and NIR wavelengths and the detailed optical spectroscopic evolution from the photospheric phase to the nebular phase ($\sim$300 days from the explosion). The various light-curve parameters were estimated,

and the peak V-band magnitude was estimated as -17.0 ± 0.1 mag. Using the bolometric light curve, the mass of synthesized radioactive ^{56}Ni is estimated as $0.026 \pm 0.007\,M_{\odot}$. The spectroscopic comparison of SN 2018gj with other Type II SNe indicated it to be a normal Type II SN but with high Hα velocities. Further, blueshift in the emission features during the late nebular phase is also reported. We carried out semianalytical modeling, nebular phase spectral comparisons, and complete 1D hydrodynamical modeling to ascertain ejecta mass, explosion energy, synthesized nickel mass, and details about the progenitor. The models favored a low-mass progenitor of ZAMS mass of $<13\,M_{\odot}$, contrary to the higher-mass RSG channels available in the literature. We found the mass of the hydrogen envelope to be only $\sim 2.5 - 3.0\,M_{\odot}$ and a total pre-SN mass $\leqslant 7\,M_{\odot}$.

Other data files, models, etc. will be shared with users upon reasonable request.

Acknowledgments

We are grateful to the anonymous referee for a thorough evaluation of the manuscript that helped in improving it. We thank the staff of IAO, Hanle, and CREST, Hosakote, that made these observations possible. The facilities at IAO and CREST are operated by the Indian Institute of Astrophysics, Bangalore. This research has made use of the High-Performance Computing (HPC) resources[9] made available by the Computer Center of the Indian Institute of Astrophysics, Bangalore. This research made use of REDPIPE[10] (Singh 2021), an assemblage of data reduction and analysis scripts written by A.S. This work was supported by the Joint Research Project, grant No. JPJSBP120227709. T.A. acknowledges support from the Egyptian Science, Technology and Innovation Funding Authority (STDF) under the grant No. 45779. D.K.S. acknowledges the support provided by the Department of Science and Technology, India (DST)-JSPS under grant No. DST/INT/JSPS/P 363/2022. This work was also partly supported by JSPS KAKENHI grant No. JP50645512. This research has also made use of the NASA/IPAC Extragalactic Database (NED[11]), which is funded by the National Aeronautics and Space Administration and operated by the California Institute of Technology. This work has used data from the Asteroid Terrestrial-impact Last Alert System (ATLAS) project. The Asteroid Terrestrial-impact Last Alert System (ATLAS) project is primarily funded to search for near-Earth asteroids through NASA grants NN12AR55G, 80NSSC18K0284, and 80NSSC18K1575; byproducts of the Near earth objects (NEO) search include images and catalogs from the survey area. This work was partially funded by Kepler/K2 grant J1944/80NSSC19K0112 and HST GO-15889, and STFC grants ST/T000198/1 and ST/S006109/1. The ATLAS science products have been made possible through the contributions of the University of Hawaii Institute for Astronomy, the Queen's University Belfast, the Space Telescope Science Institute, the South African Astronomical Observatory, and The Millennium Institute of Astrophysics (MAS), Chile.

Facilities: IAO (HCT), 2 m; Kanata (HONIR), 1.5 m; ATLAS; andSwift (UVOT).

Software: Astropy (Astropy Collaboration et al. 2013, 2018, 2022), emcee (Foreman-Mackey et al. 2013), MESA (Paxton et al. 2011, 2013, 2015, 2018, 2019), STELLA (Blinnikov & Sorokina 2004; Baklanov et al. 2005; Blinnikov et al. 2006), matplotlib (Hunter 2007), pandas (Wes McKinney 2010; pandas development team 2020), numpy (Harris et al. 2020), scipy (Virtanen et al. 2020), Jupyter (Kluyver et al. 2016), and seaborn (Waskom 2021).

Data Availability

The majority of data are presented in tables. The spectra files are provided as data behind the figure. The inlists used for creating MESA models and associated models are available on Zenodo under an open-source Creative Commons Attribution license: doi:10.5281/zenodo.7994631.

Appendix A
Data

Tables 3–7 provide observations data and spectra logs.

Table 3
The *UBVRI* Photometric Magnitudes of SN 2018gj

Date (yyyy-mm-dd)	JD 2458000+	Phase[a] (d)	U (mag)	B (mag)	V (mag)	R (mag)	I (mag)
2018-1-14	132.5	+4.7	14.07 ± 0.01	14.75 ± 0.01	14.71 ± 0.01	14.55 ± 0.01	14.43 ± 0.01
2018-1-16	134.5	+6.7	14.18 ± 0.01	14.84 ± 0.01	14.75 ± 0.01	14.54 ± 0.01	14.40 ± 0.01
2018-1-18	136.5	+8.7	14.24 ± 0.01	14.87 ± 0.01	14.79 ± 0.01	14.56 ± 0.01	14.46 ± 0.01
2018-1-21	139.5	+11.7	14.47 ± 0.01	15.00 ± 0.01	14.92 ± 0.01	14.68 ± 0.01	14.55 ± 0.01
2018-1-24	142.5	+14.7	14.66 ± 0.01	15.06 ± 0.01	14.92 ± 0.01	14.65 ± 0.01	14.54 ± 0.01
2018-1-25	143.5	+15.7	14.76 ± 0.01	15.14 ± 0.01	14.97 ± 0.01	14.68 ± 0.01	14.55 ± 0.01
2018-1-27	145.5	+17.7	14.92 ± 0.02	15.21 ± 0.01	14.99 ± 0.01	14.68 ± 0.01	14.55 ± 0.01
2018-2-2	151.5	+23.7	15.45 ± 0.02	15.49 ± 0.01	15.05 ± 0.01	14.70 ± 0.01	14.56 ± 0.01
2018-2-3	152.5	+24.7	15.50 ± 0.01	15.50 ± 0.01	15.05 ± 0.01	14.69 ± 0.01	14.56 ± 0.01
2018-2-6	155.5	+27.7	15.76 ± 0.02	15.61 ± 0.01	15.05 ± 0.01	14.69 ± 0.01	14.51 ± 0.01
2018-2-10	159.5	+31.7	16.09 ± 0.02	15.78 ± 0.01	15.14 ± 0.01	14.74 ± 0.01	14.57 ± 0.01
2018-02-13	162.5	+34.7	16.21 ± 0.02	15.86 ± 0.01	15.14 ± 0.01	14.74 ± 0.01	14.57 ± 0.01
2018-2-16	165.5	+37.7	16.43 ± 0.02	15.99 ± 0.01	15.23 ± 0.01	14.81 ± 0.01	14.62 ± 0.01
2018-2-18	167.5	+39.7	16.53 ± 0.02	16.05 ± 0.01	15.25 ± 0.01	14.82 ± 0.01	14.63 ± 0.01

[9] https://www.iiap.res.in/?q=facilities/computing/nova
[10] https://github.com/sPaMFouR/RedPipe
[11] https://ned.ipac.caltech.edu

Table 3
(Continued)

Date (yyyy-mm-dd)	JD 2458000+	Phase[a] (d)	*U* (mag)	*B* (mag)	*V* (mag)	*R* (mag)	*I* (mag)
2018-2-25	174.5	+46.7	16.93 ± 0.01	16.23 ± 0.01	15.33 ± 0.01	14.88 ± 0.01	14.66 ± 0.01
2018-3-07	184.5	+56.7	17.40 ± 0.01	16.51 ± 0.01	15.48 ± 0.01	15.00 ± 0.01	14.85 ± 0.01
2018-3-14	191.5	+63.7	⋯	16.70 ± 0.02	15.65 ± 0.01	15.12 ± 0.02	14.89 ± 0.01
2018-3-15	192.5	+64.7	17.99 ± 0.04	16.80 ± 0.01	15.65 ± 0.01	15.15 ± 0.02	14.88 ± 0.01
2018-3-18	195.5	+67.7	18.14 ± 0.03	16.94 ± 0.01	15.74 ± 0.01	15.23 ± 0.01	14.95 ± 0.01
2018-3-23	200.5	+72.7	18.69 ± 0.02	17.28 ± 0.01	15.99 ± 0.01	15.40 ± 0.01	15.10 ± 0.01
2018-3-30	207.5	+79.7	⋯	18.12 ± 0.02	16.66 ± 0.01	15.98 ± 0.01	15.58 ± 0.01
2018-4-02	210.5	+82.7	⋯	18.61 ± 0.02	17.11 ± 0.01	16.34 ± 0.01	15.93 ± 0.01
2018-4-3	211.5	+83.7	⋯	18.73 ± 0.02	17.20 ± 0.01	16.44 ± 0.02	16.10 ± 0.01
2018-4-7	215.5	+87.7	20.07 ± 0.05	18.87 ± 0.02	17.36 ± 0.01	16.58 ± 0.02	16.15 ± 0.02
2018-4-12	220.5	+92.7	⋯	18.91 ± 0.01	17.51 ± 0.01	16.67 ± 0.01	16.22 ± 0.01
2018-4-15	223.5	+95.7	⋯	⋯	17.53 ± 0.01	16.72 ± 0.01	16.30 ± 0.02
2018-4-21	229.5	+101.7	⋯	19.02 ± 0.01	17.60 ± 0.01	16.79 ± 0.01	16.37 ± 0.02
2018-4-27	235.5	+107.7	⋯	19.11 ± 0.03	17.70 ± 0.01	16.88 ± 0.01	16.44 ± 0.02
2018-4-28	236.5	+108.7	⋯	19.10 ± 0.03	17.68 ± 0.02	16.85 ± 0.03	16.43 ± 0.02
2018-4-29	237.5	+109.7	⋯	19.10 ± 0.02	17.68 ± 0.02	16.86 ± 0.01	16.46 ± 0.02
2018-5-13	251.5	+123.7	⋯	⋯	17.89 ± 0.01	17.02 ± 0.02	16.62 ± 0.03
2018-5-19	257.5	+129.7	⋯	⋯	17.98 ± 0.01	17.09 ± 0.01	16.68 ± 0.02
2018-5-28	266.5	+138.7	⋯	19.31 ± 0.03	18.13 ± 0.02	17.19 ± 0.02	16.79 ± 0.02
2018-6-7	276.5	+148.7	20.60 ± 0.05	19.47 ± 0.02	18.24 ± 0.01	17.30 ± 0.01	16.90 ± 0.02
2018-6-11	280.5	+152.7	⋯	⋯	18.32 ± 0.01	17.37 ± 0.01	16.91 ± 0.02
2018-6-24	293.5	+165.7	⋯	19.60 ± 0.02	18.49 ± 0.02	17.49 ± 0.01	17.05 ± 0.02
2018-6-27	296.5	+168.7	⋯	19.62 ± 0.02	18.41 ± 0.03	17.57 ± 0.01	17.12 ± 0.02
2018-6-30	299.5	+171.7	⋯	⋯ ± ⋯	18.59 ± 0.01	17.54 ± 0.01	17.11 ± 0.02
2018-7-5	304.5	+176.7	⋯	19.68 ± 0.03	18.59 ± 0.01	17.60 ± 0.01	17.20 ± 0.02
2018-8-3	334.3	+206.5	⋯	19.93 ± 0.04	19.02 ± 0.04	18.02 ± 0.02	17.60 ± 0.03
2018-10-12	403.5	+275.7	⋯	⋯ ± ⋯	19.85 ± 0.03	18.86 ± 0.04	18.60 ± 0.03
2018-10-31	423.1	+295.3	⋯	20.78 ± 0.03	20.17 ± 0.02	19.23 ± 0.05	19.01 ± 0.04

Note.
[a] With reference to the explosion date (JD 2458127.8).

(This table is available in machine-readable form.)

Table 4
Swift/UVOT Photometry for SN 2018gj

Date (yyyy-mm-dd)	JD 2458000+	Phase[a] (d)	*UVW*2 (mag)	*UVM*2 (mag)	*UVW*1 (mag)	*UVU* (mag)	*UVB* (mag)	*UVV* (mag)
2018-1-16	134.6	+6.8	14.11 ± 0.03	13.92 ± 0.03	13.75 ± 0.03	13.70 ± 0.03	14.82 ± 0.03	14.72 ± 0.04
2018-1-18	136.6	+8.8	14.55 ± 0.03	14.33 ± 0.04	14.08 ± 0.03	13.81 ± 0.03	14.83 ± 0.03	14.78 ± 0.04
2018-1-20	139.1	+11.3	15.01 ± 0.04	14.98 ± 0.06	14.51 ± 0.04	13.96 ± 0.04	14.89 ± 0.04	14.90 ± 0.06
2018-1-22	141.4	+13.6	15.50 ± 0.03	15.49 ± 0.04	14.91 ± 0.03	14.20 ± 0.03	14.95 ± 0.03	14.85 ± 0.04
2018-1-24	142.7	+14.9	⋯	⋯	⋯	14.34 ± 0.03	15.05 ± 0.03	14.87 ± 0.05

Note.
[a] With reference to the explosion date (JD 2458127.8).

(This table is available in machine-readable form.)

Table 5
The *JHKs* Photometric Magnitudes of SN 2018gj

Date (yyyy-mm-dd)	JD 2458000+	Phase[a] (days)	*Ks* (mag)	*H* (mag)	*J* (mag)
2018-1-17	136.3	+8.5	14.05 ± 0.09	⋯	14.28 ± 0.03
2018-1-19	138.4	+10.6	13.97 ± 0.04	14.15 ± 0.03	14.20 ± 0.03
2018-1-30	149.3	+21.5	13.88 ± 0.03	14.08 ± 0.03	14.20 ± 0.02
2018-2-3	153.3	+25.5	13.91 ± 0.03	14.10 ± 0.02	14.23 ± 0.02
2018-2-6	156.3	+28.5	13.85 ± 0.03	14.08 ± 0.02	14.13 ± 0.02
2018-2-7	157.3	+29.5	13.84 ± 0.02	14.02 ± 0.02	14.15 ± 0.02
2018-2-8	157.9	+30.1	13.83 ± 0.03	14.05 ± 0.02	14.16 ± 0.02
2018-2-14	164.3	+36.5	13.90 ± 0.04	14.05 ± 0.03	14.21 ± 0.02
2018-2-16	166.2	+38.4	14.00 ± 0.04	14.08 ± 0.02	14.23 ± 0.02
2018-2-21	171.2	+43.4	14.06 ± 0.04	14.14 ± 0.03	14.18 ± 0.02
2018-2-26	176.3	+48.5	13.92 ± 0.04	14.09 ± 0.03	14.24 ± 0.02
2018-2-27	177.0	+49.2	⋯	⋯	14.24 ± 0.02
2018-3-1	179.2	+51.4	14.01 ± 0.03	14.19 ± 0.02	14.32 ± 0.02
2018-3-9	187.3	+59.5	14.02 ± 0.03	14.23 ± 0.02	14.31 ± 0.02
2018-3-11	189.3	+61.5	13.96 ± 0.04	14.12 ± 0.03	14.29 ± 0.02
2018-3-12	190.3	+62.5	14.07 ± 0.04	14.19 ± 0.03	14.34 ± 0.02
2018-3-17	195.2	+67.4	14.15 ± 0.04	14.30 ± 0.02	14.41 ± 0.02
2018-3-22	200.1	+72.3	14.13 ± 0.03	14.43 ± 0.02	14.57 ± 0.02
2018-3-25	203.2	+75.4	14.30 ± 0.04	14.51 ± 0.03	14.66 ± 0.02
2018-3-28	206.1	+78.4	14.45 ± 0.05	14.62 ± 0.03	14.87 ± 0.02
2018-3-30	208.1	+80.4	14.72 ± 0.04	14.85 ± 0.03	15.06 ± 0.02
2018-4-1	210.2	+82.4	⋯	15.03 ± 0.04	15.31 ± 0.04
2018-4-2	211.2	+83.4	14.98 ± 0.08	15.09 ± 0.04	15.38 ± 0.04
2018-4-7	216.3	+88.5	15.19 ± 0.05	15.50 ± 0.03	15.77 ± 0.03
2018-4-8	217.2	+89.4	⋯	15.47 ± 0.04	15.74 ± 0.03
2018-4-12	221.3	+93.5	15.28 ± 0.05	15.56 ± 0.04	15.9 ± 0.04
2018-4-15	224.3	+96.5	15.25 ± 0.09	15.62 ± 0.05	15.93 ± 0.04
2018-4-17	226.3	+98.5	15.37 ± 0.09	15.57 ± 0.04	15.91 ± 0.03
2018-4-21	230.3	+102.5	⋯	15.69 ± 0.05	15.94 ± 0.04
2018-4-22	231.3	+103.5	15.43 ± 0.09	15.63 ± 0.05	15.98 ± 0.04
2018-4-28	237.2	+109.4	15.48 ± 0.10	15.79 ± 0.07	16.08 ± 0.06
2018-4-30	239.2	+111.4	15.47 ± 0.13	15.82 ± 0.07	⋯
2018-5-9	248.2	+120.4	15.74 ± 0.11	16.08 ± 0.06	16.36 ± 0.03
2018-5-11	250.1	+122.3	15.68 ± 0.12	16.05 ± 0.05	16.38 ± 0.05
2018-5-12	251.2	+123.4	⋯	⋯	16.42 ± 0.05
2018-5-21	260.1	+132.3	15.87 ± 0.16	16.48 ± 0.05	16.57 ± 0.04
2018-5-23	262.2	+134.4	15.91 ± 0.12	16.50 ± 0.07	16.66 ± 0.04
2018-5-31	270.2	+142.4	16.17 ± 0.11	16.67 ± 0.07	16.79 ± 0.06
2018-6-4	274.2	+146.4	16.23 ± 0.27	⋯	16.76 ± 0.08
2018-6-16	286.1	+158.3	16.84 ± 0.20	17.02 ± 0.12	16.91 ± 0.04
2018-7-12	312.1	+184.3	⋯	17.64 ± 0.23	⋯
2018-8-1	332.0	+204.2	⋯	⋯	17.97 ± 0.09

Note.
[a] With reference to the explosion date (JD 2458127.8).

(This table is available in machine-readable form.)

Table 6
Log of Spectroscopic Observations of SN 2018gj

Date (yyyy-mm-dd)	JD (2458000+)	Phase (days)	Range (Å)
2018-1-14	132.5	+4.7	3500–9250
2018-1-16	134.5	+6.7	3500–9250
2018-1-18	136.5	+8.7	3500–9250
2018-1-21	139.5	+11.7	3500–9250
2018-1-24	142.5	+13.7	3500–9250
2018-1-25	143.5	+15.7	3500–9250
2018-1-27	145.5	+17.7	3500–9250
2018-2-2	151.5	+23.7	3500–9250
2018-2-3	152.5	+24.7	3500–9250
2018-2-6	155.5	+27.7	3500–9250
2018-2-13	162.5	+34.7	3500–9250
2018-2-16	165.5	+37.7	3500–9250
2018-2-18	167.5	+39.7	3500–9250
2018-2-20	169.5	+41.7	3500–9250
2018-2-25	174.5	+46.7	3500–9250
2018-3-14	191.5	+63.7	3500–9250
2018-3-15	192.5	+64.7	3500–9250
2018-3-18	195.5	+67.7	3500–9250
2018-3-23	200.5	+72.7	3500–9250
2018-3-30	207.5	+79.7	3500–9250
2018-4-2	210.5	+82.7	3500–9250
2018-4-7	215.5	+87.7	3500–9250
2018-4-15	223.5	+95.7	3500–7800
2018-4-21	229.5	+101.7	3500–9250
2018-4-27	235.5	+107.7	3500–9250
2018-5-01	239.5	+111.7	3500–9250
2018-5-28	266.5	+138.7	3500–9250
2018-6-11	280.5	+152.7	3500–7800
2018-6-29	297.5	+168.7	3500–9250
2018-10-04	396.1	+268.3	5200–9250
2018-10-31	423.1	+295.3	3500–7800

Note. * With reference to the explosion date (JD 2458127.8).

Table 7
Type II SN Data Used in Comparison and Estimating Mean Color Evolution

Serial No.	SN	Reference
1	1992H	Clocchiatti et al. (1996)
2	1992af	Anderson et al. (2014a)
3	1992ba	Anderson et al. (2014a)
4	1997D	Hamuy (2003)
5	1999em	Anderson et al. (2014a)
6	1999gi	Leonard et al. (2002b)
7	2000cb	Kleiser et al. (2011)
8	2002hx	Anderson et al. (2014a)
9	2003gd	Anderson et al. (2014a)
10	2004dj	Zhang et al. (2006)
11	2004et	Sahu et al. (2006)
12	2004fx	Anderson et al. (2014a)
13	2005af	Anderson et al. (2014a)
14	2005cs	Pastorello et al. (2006)
15	2006V	Taddia et al. (2012)
16	2006au	Taddia et al. (2012)
17	2007it	Anderson et al. (2014a)
18	2007pk	Inserra et al. (2013)
19	2008gz	Roy et al. (2011)
20	2008in	Anderson et al. (2014a)
21	2009E	Pastorello et al. (2012)
22	2009N	Anderson et al. (2014a)
23	2009bw	Inserra et al. (2012)

Table 7
(Continued)

Serial No.	SN	Reference
24	2009ib	Takáts et al. (2015)
25	2009md	Fraser et al. (2011)
26	2012A	Inserra et al. (2012)
27	2012aw	Bose et al. (2013)
28	2012ec	Barbarino et al. (2015)
29	2013K	Tomasella et al. (2018)
30	2013ab	Valenti et al. (2016)
31	2013by	Valenti et al. (2016)
32	2013fs	Valenti et al. (2016)
33	LSQ13dpa	Valenti et al. (2016)
34	2013hj	Bose et al. (2016)
35	2014G	Valenti et al. (2016)
36	2014cx	Valenti et al. (2016)
37	2014dw	Valenti et al. (2016)
38	ASASSN-14 ha	Valenti et al. (2016)
39	2016X	Huang et al. (2018)
40	2016bkv	Nakaoka et al. (2018)
41	2017eaw	Tsvetkov et al. (2018)
42	2018ivc	Bostroem et al. (2020)
43	2018zd	Zhang et al. (2020)
44	2020jfo	Teja et al. (2022)
…	…	…

Appendix B
EPM Distance to SN 2018gj

The implementation of EPM was followed as per the details given in Hamuy et al. (2001), Dessart & Hillier (2005). This formalism involves the measurements of two radii associated with SN (i) a photometric angular radius (θ) and (ii) a spectroscopic physical radius (R). With the aid of these two radii, the distance to SN could be derived. The angular radius (θ) is given as follows:

$$\theta = \frac{R}{D} = \sqrt{\frac{f_\lambda}{\pi B_\lambda(T)\, 10^{-0.4A(\lambda)}\, \zeta_\lambda^2}};$$

where D is the distance to the SN. $B_\lambda(T)$ is the Planck function at the color temperature of the blackbody radiation, f_λ is the apparent flux density, $A(\lambda)$ is the dust extinction, and ζ_λ is the dilution factor to account for the deviation from a blackbody (Hamuy et al. 2001). The above equation could be transformed in terms of apparent magnitudes (m_λ) for multiband photometry as follows:

$$\mathrm{m}_\lambda = -5\log(\zeta_\lambda) - 5\log(\theta) + \mathrm{A}_\lambda + \mathrm{b}_\lambda(\mathrm{T}).$$

Now, for the different filters set (S) above, the equation was minimized with b_λ values being taken from Hamuy et al. (2001), and the dilution factors have been considered from three different works, viz., Hamuy et al. (2001), Dessart & Hillier (2005), and Vogl et al. (2019). The quantity that was minimized is as follows:

$$\varepsilon = \sum_{\lambda \epsilon S} [m_\lambda + log(\theta_S \zeta_S) - A_\lambda - b_\lambda(T_S)]^2 .$$

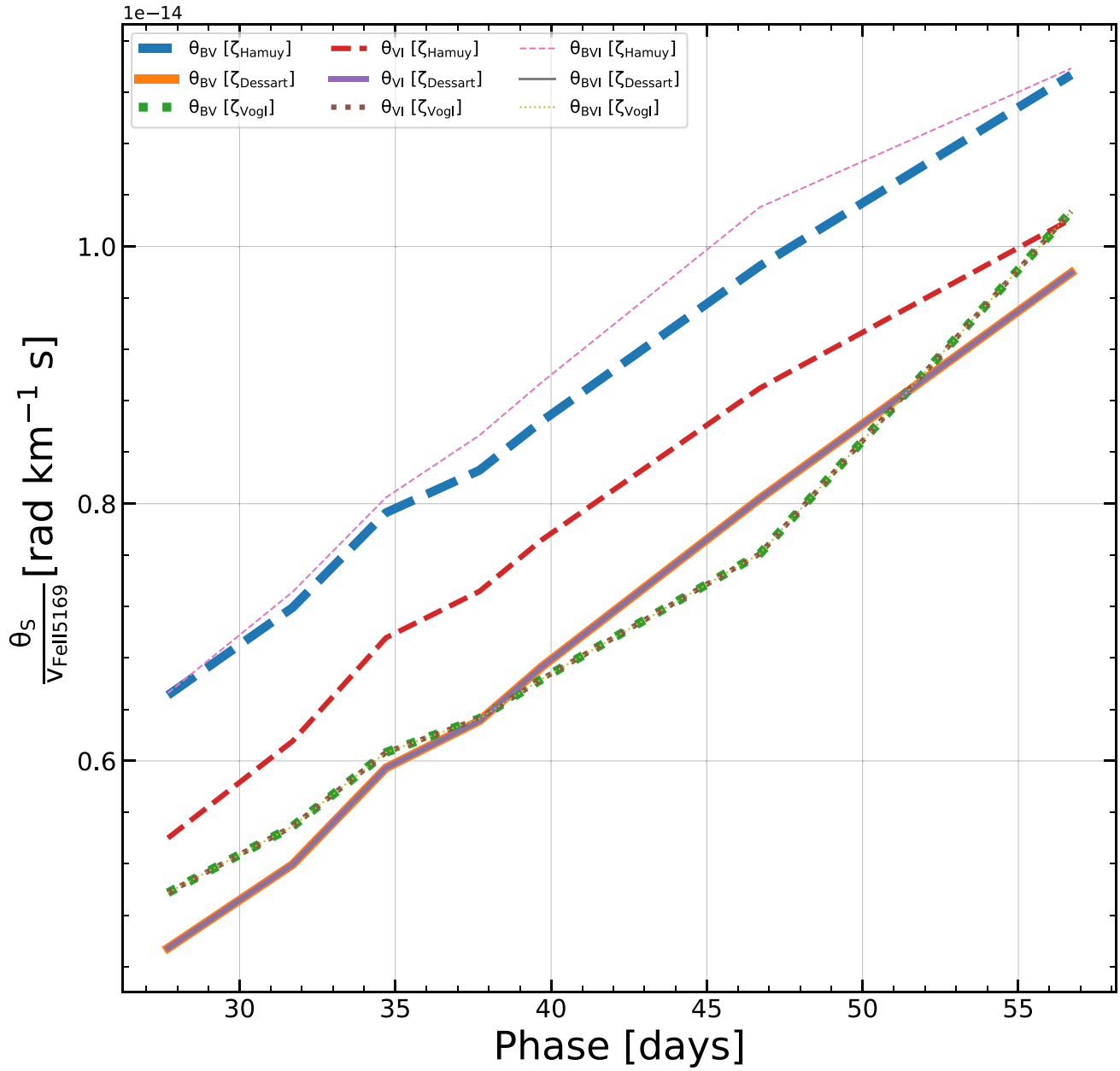

Figure 21. EPM distance estimates for various filter sets and different dilution factors from Hamuy et al. (2001), Dessart & Hillier (2005), and Vogl et al. (2019).

Finally, using the expansion velocity (v) measured using spectra could be used in the following equation:

$$\frac{\theta_i}{v_i} \approx \frac{(t_i - t_0)}{D};$$

where subscript i implies for each epoch available. A straight line could be fit for multiple epochs, and the resulting slope is used to get estimates of the distance (See Figure 21).

Appendix C
Scaling Relation for Probable Progenitor

The scaling relations obtained in Goldberg et al. (2019) that give a set of probable explosions that could yield an observed bolometric light curve can be used for the initial model guess in MESA models (Figure 22). These relations are solved to obtain $M_{\rm ej}$ and $E_{\rm exp}$ as a function of $M_{\rm Ni}$, L_{50}, t_p, and R as follows:

$$\log(E_{51}) = -0.728 + 2.148\log(L_{42}) - 0.280\log(M_{Ni}) + 2.091\log(t_{p,2}) - 1.632\log(R_{500}), \quad \text{(C1)}$$

and

$$\log(M_{10}) = -0.947 + 1.474\log(L_{42}) - 0.518\log(M_{Ni}) + 3.867\log(t_{p,2}) - 1.120\log(R_{500}), \quad \text{(C2)}$$

where E_{51} is explosion energy in the units 10^{51} ergs, M_{10} is the ejecta mass in the units $10\,M_\odot$, $M_{\rm Ni}$ has $M_\odot$ unit, L_{42} = luminosity at 50 days/10^{42} erg s^{-1}, R_{500} = progenitor radius/$500\,R_\odot$, and $t_{p,2}$ = plateau length/100 days.

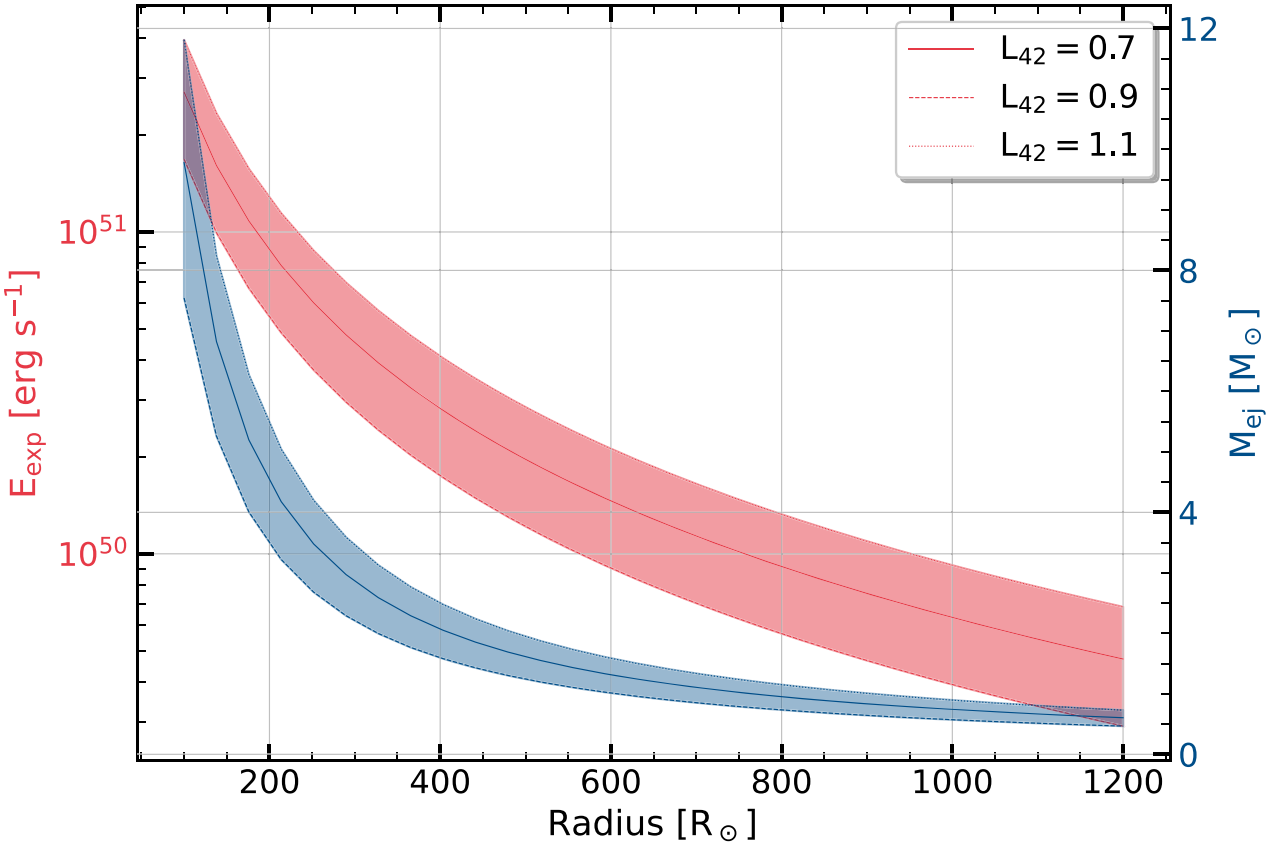

Figure 22. Scaling relations (Goldberg et al. 2019) in the context of Type IIP SNe as applicable to SN 2018gj.

Appendix D
Model Light Curves and Velocity Evolution for 19 $M_\odot$ Models

Figure 23 gives the model light curves for 19 $M_\odot$ models.

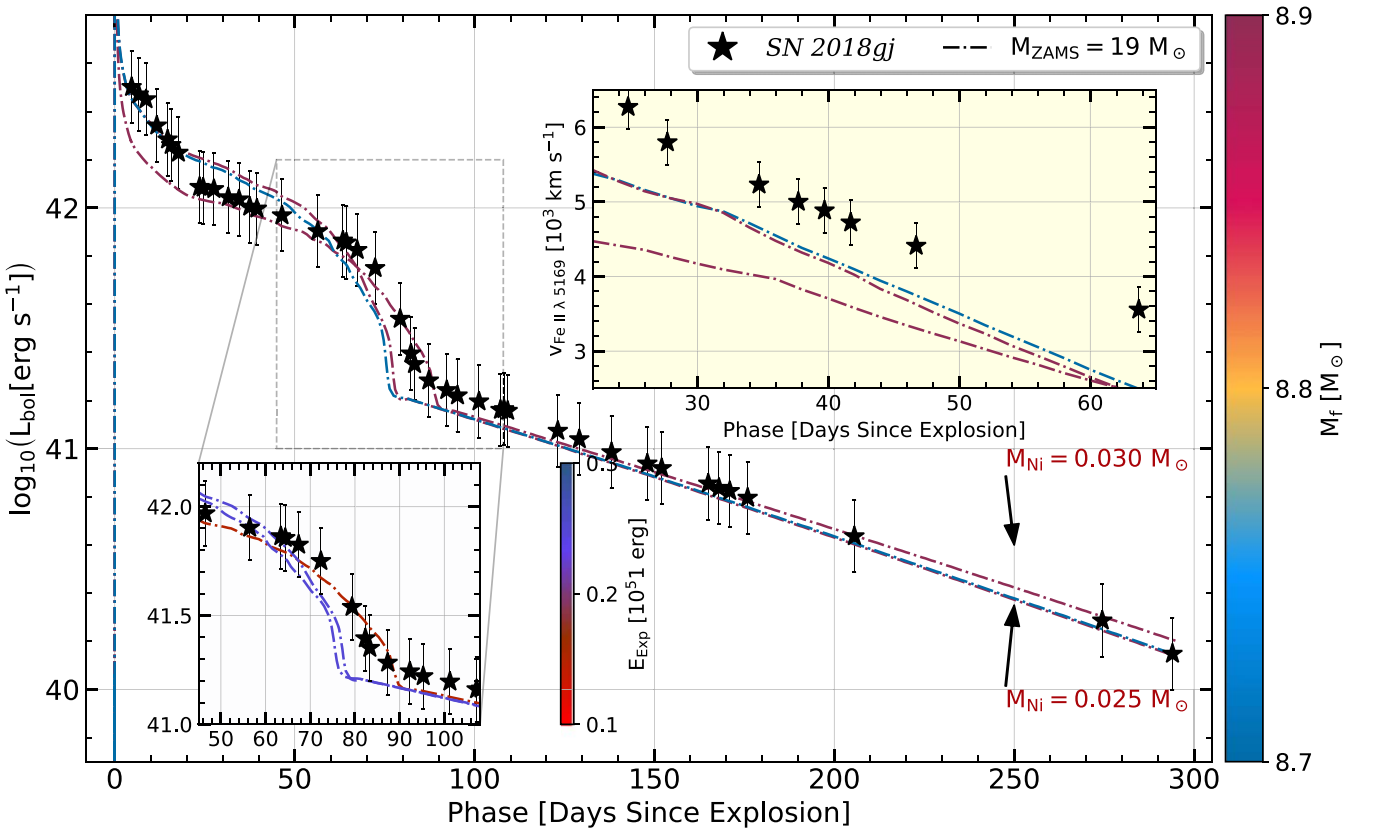

Figure 23. Variations in 19 $M_{\odot}$ ZAMS model using different parameters to achieve a shorter plateau length. Zoomed out, a plot in the bottom left shows the variation in explosion energy for different model light curves around the plateau transition. The second plot in the right inset shows the corresponding Fe 5169 velocities obtained using models. All the 19 $M_{\odot}$ models underestimate the velocity evolution.

ORCID iDs

Rishabh Singh Teja https://orcid.org/0000-0002-0525-0872
Avinash Singh https://orcid.org/0000-0003-2091-622X
D. K. Sahu https://orcid.org/0000-0002-6688-0800
G. C. Anupama https://orcid.org/0000-0003-3533-7183
Brajesh Kumar https://orcid.org/0000-0001-7225-2475
Koji S Kawabata https://orcid.org/0000-0001-6099-9539
Masayuki Yamanaka https://orcid.org/0000-0001-9456-3709
Ali Takey https://orcid.org/0000-0003-1423-5516
Miho Kawabata https://orcid.org/0000-0002-4540-4928

References

Akitaya, H., Moritani, Y., Ui, T., et al. 2014, Proc. SPIE, 9147, 91474O
Anderson, J. P., Dessart, L., Gutierrez, C. P., et al. 2014b, MNRAS, 441, 671
Anderson, J. P., González-Gaitán, S., Hamuy, M., et al. 2014a, ApJ, 786, 67
Andrews, J. E., Sand, D. J., Valenti, S., et al. 2019, ApJ, 885, 43
Andrews, J. E., Sugerman, B. E. K., Clayton, G. C., et al. 2011, ApJ, 731, 47
Angulo, C. 1999, in AIP Conf. Ser. 495, Experimental Nuclear Physics in Europe: Facing the Next Millennium (Melville, NY: AIP), 365
Arcavi, I., Gal-Yam, A., Cenko, S. B., et al. 2012, ApJL, 756, L30
Arnett, W. D., & Fu, A. 1989, ApJ, 340, 396
Astropy Collaboration, Price-Whelan, A. M., Lim, P. L., et al. 2022, ApJ, 935, 167
Astropy Collaboration, Price-Whelan, A. M., Sipőcz, B. M., et al. 2018, AJ, 156, 123
Astropy Collaboration, Robitaille, T. P., Tollerud, E. J., et al. 2013, A&A, 558, A33
Baklanov, P. V., Blinnikov, S. I., & Pavlyuk, N. N. 2005, AstL, 31, 429
Barbarino, C., Dall'Ora, M., Botticella, M. T., et al. 2015, MNRAS, 448, 2312
Barbon, R., Ciatti, F., & Rosino, L. 1979, A&A, 72, 287
Bellm, E. C., Kulkarni, S. R., Graham, M. J., et al. 2019, PASP, 131, 018002
Bertrand, E. 2018, TNSCR 2018-56, 1
Bessell, M. S., Castelli, F., & Plez, B. 1998, A&A, 333, 231
Blinnikov, S., & Sorokina, E. 2004, Ap&SS, 290, 13
Blinnikov, S. I., & Popov, D. V. 1993, A&A, 274, 775
Blinnikov, S. I., Röpke, F. K., Sorokina, E. I., et al. 2006, A&A, 453, 229
Bose, S., Kumar, B., Misra, K., et al. 2016, MNRAS, 455, 2712
Bose, S., Kumar, B., Sutaria, F., et al. 2013, MNRAS, 433, 1871
Bose, S., Valenti, S., Misra, K., et al. 2015, MNRAS, 450, 2373
Bostroem, K. A., Valenti, S., Sand, D. J., et al. 2020, ApJ, 895, 31
Bottinelli, L., Gouguenheim, L., Paturel, G., & de Vaucouleurs, G. 1984, A&AS, 56, 381
Brown, P. J., Holland, S. T., Immler, S., et al. 2009, AJ, 137, 4517
Bruch, R. J., Gal-Yam, A., Yaron, O., et al. 2023, ApJ, 952, 119
Bullivant, C., Smith, N., Williams, G. G., et al. 2018, MNRAS, 476, 1497
Cardelli, J. A., Clayton, G. C., & Mathis, J. S. 1989, ApJ, 345, 245
Chatzopoulos, E., Wheeler, J. C., & Vinko, J. 2012, ApJ, 746, 121
Chugai, N. N. 1988, SvAL, 14, 334
Clocchiatti, A., Benetti, S., Wheeler, J. C., et al. 1996, AJ, 111, 1286
Curtis, S., Wolfe, N., Fröhlich, C., et al. 2021, ApJ, 921, 143
Cyburt, R. H., Amthor, A. M., Ferguson, R., et al. 2010, ApJS, 189, 240
Dastidar, R., Misra, K., Hosseinzadeh, G., et al. 2018, MNRAS, 479, 2421
Davies, B., & Beasor, E. R. 2020, MNRAS Lett., 496, L142
de Jaeger, T., Zheng, W., Stahl, B. E., et al. 2019, MNRAS, 490, 2799
Dessart, L., & Hillier, D. J. 2005, A&A, 439, 671
Dessart, L., & Hillier, D. J. 2022, A&A, 660, L9
Dessart, L., Hillier, D. J., Waldman, R., & Livne, E. 2013, MNRAS, 433, 1745
Dessart, L., Livne, E., & Waldman, R. 2010, MNRAS, 408, 827
Dong, Y., Valenti, S., Bostroem, K. A., et al. 2021, ApJ, 906, 56
Duffell, P. C. 2016, ApJ, 821, 76
Eldridge, J. J., Fraser, M., Smartt, S. J., Maund, J. R., & Crockett, R. M. 2013, MNRAS, 436, 774
Eldridge, J. J., Xiao, L., Stanway, E. R., Rodrigues, N., & Guo, N. Y. 2018, PASA, 35, e049
Elmhamdi, A., Chugai, N. N., & Danziger, I. J. 2003a, A&A, 404, 1077
Elmhamdi, A., Danziger, I. J., Chugai, N., et al. 2003b, MNRAS, 338, 939
Evans, K. A., & Massey, P. 2015, AJ, 150, 149
Faran, T., Poznanski, D., Filippenko, A. V., et al. 2014a, MNRAS, 442, 844

Faran, T., Poznanski, D., Filippenko, A. V., et al. 2014b, MNRAS, 445, 554
Farmer, R., Fields, C. E., Petermann, I., et al. 2016, ApJS, 227, 22
Filippenko, A. V. 1997, ARA&A, 35, 309
Foreman-Mackey, D., Hogg, D. W., Lang, D., & Goodman, J. 2013, PASP, 125, 306
Fransson, C., & Chevalier, R. A. 1989, ApJ, 343, 323
Fraser, M., Ergon, M., Eldridge, J. J., et al. 2011, MNRAS, 417, 1417
Gaia Collaboration, Prusti, T., de Bruijne, J. H. J., et al. 2016, A&A, 595, A1
Galbany, L., Hamuy, M., Phillips, M. M., et al. 2016, AJ, 151, 33
Gal-Yam, A., Arcavi, I., Ofek, E. O., et al. 2014, Natur, 509, 471
Gangopadhyay, A., Turatto, M., Benetti, S., et al. 2020, MNRAS, 499, 129
Gehrels, N., Chincarini, G., Giommi, P., et al. 2004, ApJ, 611, 1005
Glebbeek, E., Gaburov, E., de Mink, S. E., Pols, O. R., & Portegies Zwart, S. F. 2009, A&A, 497, 255
Goldberg, J. A., Bildsten, L., & Paxton, B. 2019, ApJ, 879, 3
Goldberg, J. A., Jiang, Y.-F., & Bildsten, L. 2022, ApJ, 933, 164
Gutiérrez, C. P., Anderson, J. P., Hamuy, M., et al. 2017, ApJ, 850, 89
Hamuy, M. 2003, ApJ, 582, 905
Hamuy, M., Pinto, P. A., Maza, J., et al. 2001, ApJ, 558, 615
Harris, C. R., Millman, K. J., van der Walt, S. J., et al. 2020, Natur, 585, 357
Henyey, L., Vardya, M. S., & Bodenheimer, P. 1965, ApJ, 142, 841
Hiramatsu, D., Howell, D. A., Moriya, T. J., et al. 2021, ApJ, 913, 55
Horne, K. 1986, PASP, 98, 609
Huang, F., Wang, X. F., Hosseinzadeh, G., et al. 2018, MNRAS, 475, 3959
Hunter, J. D. 2007, CSE, 9, 90
Inserra, C., Pastorello, A., Turatto, M., et al. 2013, A&A, 555, A142
Inserra, C., Turatto, M., Pastorello, A., et al. 2012, MNRAS, 422, 1122
Jerkstrand, A. 2017a, in Handbook of Supernovae, ed. A. W. Alsabti & P. Murdin (Cham: Springer), 795
Jerkstrand, A. 2017b, in Handbook of Supernovae, ed. A. W. Alsabti & P. Murdin (Cham: Springer), 1
Jerkstrand, A., Smartt, S. J., Fraser, M., et al. 2014, MNRAS, 439, 3694
Khazov, D., Yaron, O., Gal-Yam, A., et al. 2016, ApJ, 818, 3
Kilpatrick, C. 2018, TNSCR 2018-2075, 1
Kirshner, R. P., & Kwan, J. 1974, ApJ, 193, 27
Kleiser, I. K. W., Poznanski, D., Kasen, D., et al. 2011, MNRAS, 415, 372
Kluyver, T., Ragan-Kelley, B., Pérez, F., et al. 2016, in Positioning and Power in Academic Publishing: Players, Agents and Agendas, ed. F. Loizides & B. Scmidt (Amsterdam: IOS Press), 87
Kochanek, C. S. 2020, MNRAS, 493, 4945
Kochanek, C. S., Shappee, B. J., Stanek, K. Z., et al. 2017, PASP, 129, 104502
Landolt, A. U. 1992, AJ, 104, 340
Leonard, D. C., Filippenko, A. V., Gates, E. L., et al. 2002a, PASP, 114, 35
Leonard, D. C., Filippenko, A. V., Li, W., et al. 2002b, AJ, 124, 2490
Minkowski, R. 1941, PASP, 53, 224
mnicholl 2018, mnicholl/superbol: superbol v1.0, Zenodo, doi:10.5281/zenodo.2155821
Morozova, V., Piro, A. L., & Valenti, S. 2018, ApJ, 858, 15
Nagy, A. P., Ordasi, A., Vinkó, J., & Wheeler, J. C. 2014, A&A, 571, A77
Nagy, A. P., & Vinkó, J. 2016, A&A, 589, A53
Nakaoka, T., Kawabata, K. S., Maeda, K., et al. 2018, ApJ, 859, 78
Nugis, T., & Lamers, H. J. G. L. M. 2000, A&A, 360, 227
pandas development team, T. 2020, pandas-dev/pandas: Pandas, latest, Zenodo, doi:10.5281/zenodo.3509134
Pastorello, A., Pumo, M. L., Navasardyan, H., et al. 2012, A&A, 537, A141
Pastorello, A., Sauer, D., Taubenberger, S., et al. 2006, MNRAS, 370, 1752
Pastorello, A., Valenti, S., Zampieri, L., et al. 2009, MNRAS, 394, 2266
Patat, F., Cappellaro, E., Danziger, J., et al. 2001, ApJ, 555, 900
Paxton, B., Bildsten, L., Dotter, A., et al. 2011, ApJS, 192, 3
Paxton, B., Cantiello, M., Arras, P., et al. 2013, ApJS, 208, 4
Paxton, B., Marchant, P., Schwab, J., et al. 2015, ApJS, 220, 15
Paxton, B., Schwab, J., Bauer, E. B., et al. 2018, ApJS, 234, 34
Paxton, B., Smolec, R., Schwab, J., et al. 2019, ApJS, 243, 10
Pessi, P. J., Folatelli, G., Anderson, J. P., et al. 2019, MNRAS, 488, 4239
Poole, T. S., Breeveld, A. A., Page, M. J., et al. 2008, MNRAS, 383, 627
Popov, D. V. 1993, ApJ, 414, 712
Poznanski, D., Prochaska, J. X., & Bloom, J. S. 2012, MNRAS, 426, 1465
Prabhu, T. P. 2014, PINSA, 80, 887
Ransome, C. L., Habergham-Mawson, S. M., Darnley, M. J., James, P. A., & Percival, S. M. 2022, MNRAS, 513, 3564
Rodrigo, C., & Solano, E. 2020, XIV.0 Scientific Meeting (Virtual) of the Spanish Astronomical Society, 182
Rodrigo, C., Solano, E., & Bayo, A. 2012, SVO Filter Profile Service Version 1.0, IVOA Working Draft 15 October 2012, International Virtual Observatory Alliance, https://www.ivoa.net/documents/Notes/SVOFPS/index.html
Rodríguez, Ó. 2022, MNRAS, 515, 897
Roming, P. W. A., Kennedy, T. E., Mason, K. O., et al. 2005, SSRv, 120, 95
Roy, R., Kumar, B., Moskvitin, A. S., et al. 2011, MNRAS, 414, 167
Rubin, A., Gal-Yam, A., De Cia, A., et al. 2016, ApJ, 820, 33
Sahu, D. K., Anupama, G. C., Srividya, S., & Muneer, S. 2006, MNRAS, 372, 1315
Sanders, N. E., Soderberg, A. M., Gezari, S., et al. 2015, ApJ, 799, 208
Schlafly, E. F., & Finkbeiner, D. P. 2011, ApJ, 737, 103
Schmidt, B. P., Kirshner, R. P., & Eastman, R. G. 1992, ApJ, 395, 366
Sim, S. A. 2017, in Handbook of Supernovae, ed. A. W. Alsabti & P. Murdin (Cham: Springer), 769
Singh, A. 2021, RedPipe: Reduction Pipeline, Astrophysics Source Code Library, ascl:2106.024
Singh, A., Kumar, B., Moriya, T. J., et al. 2019, ApJ, 882, 68
Singh, A., Srivastav, S., Kumar, B., Anupama, G. C., & Sahu, D. K. 2018, MNRAS, 480, 2475
Skrutskie, M. F., Cutri, R. M., Stiening, R., et al. 2006, AJ, 131, 1163
Smartt, S. J. 2009, ARA&A, 47, 63
Smartt, S. J., Eldridge, J. J., Crockett, R. M., & Maund, J. R. 2009, MNRAS, 395, 1409
Smith, K. W., Smartt, S. J., Young, D. R., et al. 2020, PASP, 132, 085002
Smith, N., Mauerhan, J. C., & Prieto, J. L. 2014, MNRAS, 438, 1191
Sollerman, J., Yang, S., Schulze, S., et al. 2021, A&A, 655, A105
Spiro, S., Pastorello, A., Pumo, M. L., et al. 2014, MNRAS, 439, 2873
Stalin, C. S., Hegde, M., Sahu, D. K., et al. 2008, BASI, 36, 111
Stetson, P. B. 1987, PASP, 99, 191
Stritzinger, M., Taddia, F., Fransson, C., et al. 2012, ApJ, 756, 173
Sukhbold, T., Ertl, T., Woosley, S. E., Brown, J. M., & Janka, H. T. 2016, ApJ, 821, 38
Taddia, F., Stritzinger, M. D., Sollerman, J., et al. 2012, A&A, 537, A140
Taddia, F., Stritzinger, M. D., Sollerman, J., et al. 2013, A&A, 555, A10
Takáts, K., Pignata, G., Pumo, M. L., et al. 2015, MNRAS, 450, 3137
Teja, R. S., Singh, A., Sahu, D. K., et al. 2022, ApJ, 930, 34
Tomasella, L., Cappellaro, E., Pumo, M. L., et al. 2018, MNRAS, 475, 1937
Tonry, J. L., Denneau, L., Heinze, A. N., et al. 2018, PASP, 130, 064505
Townsend, R. 2020, MESA SDK for Linux, 20.12.1, Zenodo, doi:10.5281/zenodo.4587206
Tsvetkov, D. Y., Shugarov, S. Y., Volkov, I. M., et al. 2018, AstL, 44, 315
Tutui, Y., & Sofue, Y. 1997, A&A, 326, 915
Valenti, S., Howell, D. A., Stritzinger, M. D., et al. 2016, MNRAS, 459, 3939
Valenti, S., Sand, D., Pastorello, A., et al. 2014, MNRAS Lett., 438, L101
Van Dyk, S. D. 2017, RSPTA, 375, 20160277
Vink, J. S., de Koter, A., & Lamers, H. J. G. L. M. 2001, A&A, 369, 574
Virtanen, P., Gommers, R., Oliphant, T. E., et al. 2020, NatMe, 17, 261
Vogl, C., Sim, S. A., Noebauer, U. M., Kerzendorf, W. E., & Hillebrandt, W. 2019, A&A, 621, A29
Waskom, M. L. 2021, JOSS, 6, 3021
Wes McKinney 2010, in Proc. 9th Python in Science Conf., ed. S. van der Walt & J. Millman, 56
Wiggins, P. 2018, TNSTR, 2018-53, 1
Yang, S., Sollerman, J., Strotjohann, N. L., et al. 2021, A&A, 655, A90
Zhang, J., Wang, X., József, V., et al. 2020, MNRAS, 498, 84
Zhang, T., Wang, X., Li, W., et al. 2006, AJ, 131, 2245
Zhang, X., Wang, X., Sai, H., et al. 2022, MNRAS, 509, 2013